1

FLUORESCENCE

DAVID J. S. BIRCH, YU CHEN, AND OLAF J. ROLINSKI
Photophysics Group, Department of Physics, Strathclyde University, Glasgow, UK

1.1 INTRODUCTION

Within the wide range of spectroscopic techniques facilitated by photonics, fluorescence sits alongside the likes of spectrophotometry, Raman, FTIR, circular dichroism, and ultrafast in providing complementary and unique information. Although fluorescence can hardly be called a new phenomenon, there can be little doubt that it continues to facilitate many important new observations and techniques across a whole range of disciplines. Just as photonics has become an enabling technology so too fluorescence has become an enabling phenomenon. Fluorescence has made, and continues to make, particular impact in the biosciences and in healthcare. This has been dramatically demonstrated in recent years by the key role played by fluorescence in the complete sequencing of the human genome and in the displacement of radioactive markers by fluorescence probes in disease diagnostics. Underpinning the impact of fluorescence is a research base founded upon the fact that the nanosecond timescales and nanometer distances, in which the properties of fluorescence can be influenced, are ideally matched to many physiological processes and structures.

Originating from a spin-allowed singlet−singlet transition, fluorescence has a much higher quantum yield and is usually easier to study than its photophysical counterpart, phosphorescence, which involves a spin-forbidden triplet–singlet transition. Reflecting its more generic usage, and greater range of materials and conditions that facilitate fluorescence, here we concentrate on fluorescence rather than phosphorescence. Fluorescence is traditionally associated with aromatic molecules, of which there is a vast number, but recently there has been the emergence of a whole new

Photonics: Scientific Foundations, Technology and Applications, Volume IV, First Edition.
Edited by David L. Andrews.

range of complementary luminescent nanoparticle emitters fabricated from semiconductors, gold and diamond.

When the readily accessible properties of fluorescence are combined with the high sensitivity afforded by photon counting photonics, fluorescence has enabled the ultimate limit of single molecule detection to be realized and this in turn is helping to open up new frontiers, such as molecular pathology, whereby metabolism, disease, and pharmacology can be studied at the most fundamental level. Taking the perspective of fluorescence as an enabling phenomenon, we have chosen in this chapter to survey the main techniques and measurements it "enables." We cover spectra, quantum yield, lifetime, quenching, anisotropy, and microscopy, in each case citing topical review articles, many of the original references, underlying theory and modern day applications. The applications are also supported by descriptions of the context, theory, instrumentation, and techniques. Throughout we focus on the methods which are in most widespread use, while highlighting many of the most recent developments. There are already plenty of excellent general texts that survey fluorescence in the wider context of photophysics, and its related techniques, and in more depth than we do here [1–4]. Nevertheless, we hope our approach will provide a useful introduction for readers seeking to learn the basics through to the current state of the field by means of examples of what fluorescence might be able to do for them.

1.2 SPECTRA

Measuring absorption and fluorescence spectra is usually the first place to start in any fluorescence study. The origins of many of the fundamentals of fluorescence lie within spectra and although at times they might lack specificity, the importance of spectra in providing supporting information should not be overlooked when more advanced implementations of fluorescence are being undertaken.

1.2.1 Background and Theory

Fluorescence can be viewed as a multidimensional contour of intensity, wavelength, quantum yield, decay time, polarization, and position that together characterize the emitting species. Fluorescence spectra are today quite simple to measure and reveal information on the energy levels of a fluorophore, in terms of electronic (∼2–3 eV) and vibrational (∼0.01 eV) properties, that are superimposed on what is effectively a rotational continuum. All of these are capable of being influenced by the local environment, and hence, fluorescence spectra are not only a fingerprint of a molecule, but also can be used as a probe of local interactions.

The fluorescence spectroscopy of aromatic molecules is predominantly in the near ultraviolet (UV) to near-infrared (IR) (∼250–900 nm) as it is due to the excitation of weakly bound π-electrons rather than the more strongly bound σ-electrons. In general, where π-electron delocalization increases with the size of the molecule, the absorption and fluorescence spectra shift to longer wavelengths in the manner of a

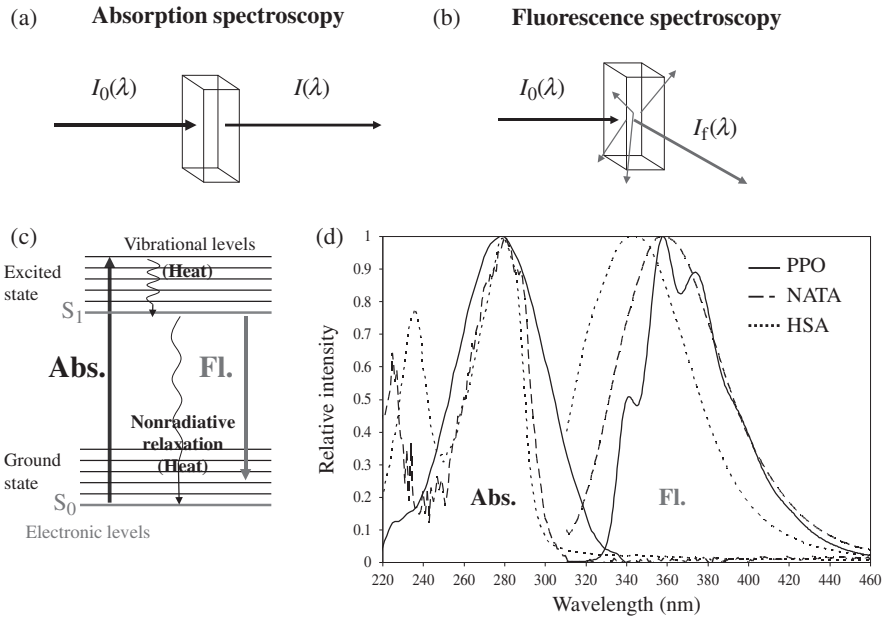

FIGURE 1.1 Geometries for the measurement of (a) absorption *(I_0 – I)* and (b) fluorescence (I_f) spectra. (c) Simplified Jablonski energy level scheme for singlet states involved in fluorescence and (d) corresponding spectra measured in condensed media. PPO refers to the scintillator 2,5-diphenyloxazole, NATA is *N*-acetyl-L-tryptophanamide, a derivative of the fluorescent amino acid tryptophan, and HSA is the protein human serum albumin, which contains a single tryptophan.

particle in a box [2]. This can often lead to a useful intuitive expectation of where spectra occur for different molecules in respect to each other before any measurement is performed.

Figure 1.1 illustrates some of the basics of fluorescence spectroscopy. Unlike the measurement of absorption spectra, which by necessity requires the incident light and transmitted light to be detected in-line, fluorescence is usually detected off-axis in order to minimize the detection of the excitation light as this would otherwise swamp the much smaller fluorescence signal. In general, fluorescence is isotropic and is usually detected at 90° to the excitation as illustrated. The energy level scheme shown in Figure 1.1 just relates to the singlet manifold and is a simplified version of the Jablonski scheme [2]. The spectra shown illustrate the fact that in condensed media fluorescence occurs from the lowest vibrational level of the lowest electronic excited state S_1 to vibrational levels of the S_0 electronic ground state (Kasha's rule [2]). Therefore, whereas absorption spectra contain information on the vibrational spacing of the excited state, fluorescence spectra contain information on the vibrational spacing of ground state. The fact that vibrational levels, although quantized, are not well resolved is due to the spectral smearing generated by rotational modes of lower energy. Taken together these properties result in fluorescence being

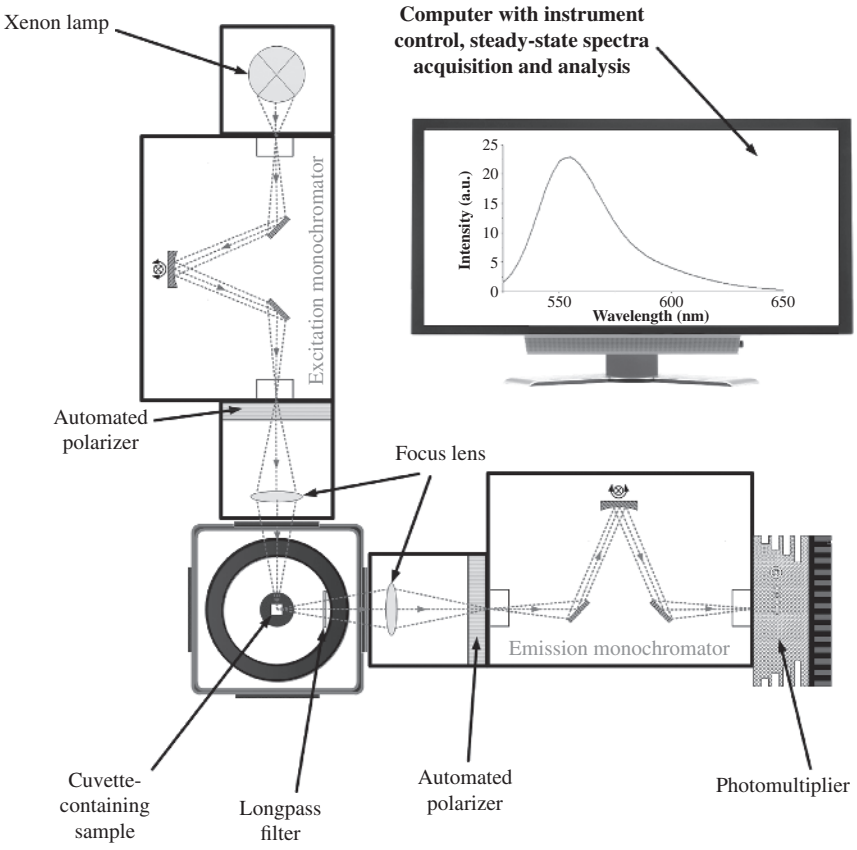

FIGURE 1.2 Typical fluorimeter schematic for recording excitation and fluorescence spectra.

shifted to longer wavelengths as compared to absorption, the so-called Stokes shift, with both spectra often displaying mirror image symmetry across their overlap [1].

1.2.2 Experimental

Figure 1.2 shows the common L-format configuration of a fluorimeter for recording fluorescence spectra. It comprises a xenon source, excitation monochromator (e.g., Seya-Namioka geometry as shown here or Czerny-Turner), sample compartment, emission monochromator, and photomultiplier detector. Further optical components, either lenses or mirrors, for focusing are required in order to match the cone angles of the excitation and fluorescence to the monochromator *f* number. Polarizers, either dichroic for the visible or quartz prisms to extend down to the UV, are sometimes added (e.g., for use in anisotropy studies—see Section 1.6). Fluorescence spectra are usually corrected for the spectral response of the emission monochromator and detecting photomultiplier, by division of this combined instrumental function.

This configuration can also be used to record excitation spectra by keeping the monochromator tuned to an emission wavelength while scanning the excitation monochromator wavelength λ. For an optically dilute sample, the excitation spectrum is equivalent to the sample's absorption spectrum. From the Beer–Lambert law,

$$I(\lambda) = I_0(\lambda)\, 10^{-\varepsilon(\lambda)cd}, \tag{1.1}$$

where I is the transmitted intensity after sample absorption, I_0 the incident intensity, c the molar concentration in mol L^{-1} (M), d the sample path length in cm, and $\varepsilon(\lambda)$ the decadic molar extinction coefficient in mol^{-1} L cm^{-1}, the ordinate in an absorption spectrum and the molecular fingerprint which is described by the spectral shape. $\varepsilon(\lambda)cd$ is defined as the optical density or absorbance of the sample.

In the limit of dilute solution, defined as $\varepsilon(\lambda)cd \ll 1$, and defining the fluorescence quantum yield Φ_f as the ratio of the rate of total fluorescence emission I_f to the rate of absorption:

$$\Phi_f = I_f/(I_0 - I), \tag{1.2}$$

we obtain [5]

$$I_f = 2.303\Phi_f \varepsilon(\lambda)\, cd. \tag{1.3}$$

Because Φ_f is usually independent of excitation wavelength for aromatic molecules in condensed media, Eq. (1.3) shows how detecting fluorescence (even at only one emission wavelength), while scanning the excitation wavelength, leads to an excitation spectrum that is equivalent to the absorption spectrum for dilute solutions because $I_f \propto \varepsilon(\lambda)$. In the case of absorption, the spectrophotometer used to measure spectra automatically corrects for the spectral distribution of the light source, the spectral response of the monochromator and detecting photomultiplier, by dividing the two signals generated in a dual beam arrangement of sample and reference channels. By similar means fluorescence excitation spectra need to be corrected for the light source spectral output and the excitation monochromator spectral response. In this regard, rhodamine B in ethylene glycol has long been used as a quantum counter [6] as its fluorescence yield is independent of excitation wavelength in the range 220–600 nm and this overcomes the wavelength response of the photomultiplier. The limit of detection for fluorescence is orders of magnitude lower than that of absorption (e.g., $\sim 10^{-12}$ M compared to 10^{-8} M) because the latter ultimately relies upon measuring a small difference between two large signals in the sample and reference channel. Fluorescence on the other hand compares a signal with zero signal or low background, which is a much easier measurement.

1.2.3 Application Example—Melanin Spectra

In order to illustrate how absorption and fluorescence spectra often interplay in tandem, we consider the example of the auto-oxidation of 3,4-dihydroxy-L-phenylalanine (L-DOPA) to produce melanin (Fig. 1.3). L-DOPA is a small molecule as aromatics go, but during its auto-oxidation a complex series of intermediaries are

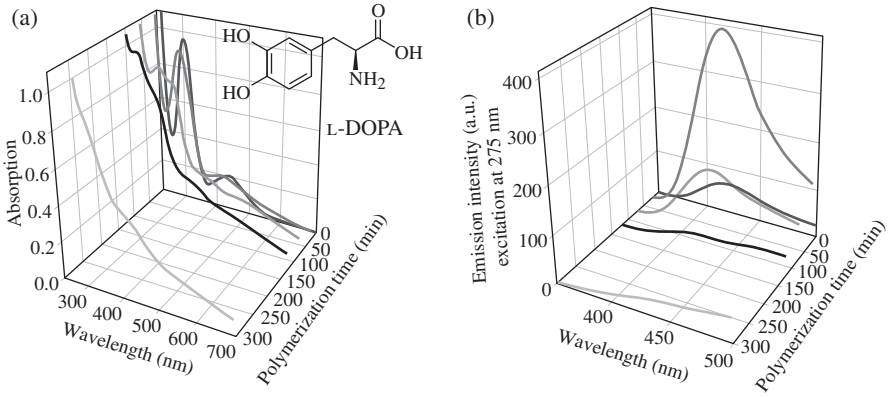

FIGURE 1.3 (a) Absorption and (b) fluorescence spectra as eumelanin is polymerized from the auto-oxidation of an aqueous solution of L-DOPA at pH 12. The fluorescence excitation wavelength is 275 nm. (*For a color version of this figure, see the color plate section.*)

formed before an extended structure, believed to bear a close similarity to natural eumelanin, is formed [7].

Initially the phenyl ring of L-DOPA is seen to dominate the absorption spectrum with a peak occurring below 300 nm, similar to that for benzene, toluene, and the three fluorescent amino acids phenylalanine, tyrosine, and tryptophan. At these times, the fluorescence is quite strong. However, as time progresses, more extended structures are formed to give the characteristically broad band attenuation spectrum of melanin describing the photoprotective action of melanin and the 275-nm excitation generates less fluorescence as the excitation energy is dissipated nonradiatively [8]. Ideally it is preferable to use intrinsic fluorescence to report on structure. This is because it does not distort native structure as extrinsic fluorescence probes can do. However, complex heterostructures such as melanin usually contain multiple fluorophores and give a complex intrinsic fluorescence signature that is difficult to interpret. The same is true of the many types of protein that contain multiple fluorescent amino acids.

1.3 QUANTUM YIELD

Measuring absolute fluorescence quantum yield is not so common an objective these days since most of the fundamental processes of aromatic are well-established and the focus of fluorescence has shifted more toward biological molecules, where their natural environment is usually saturated with the quencher oxygen. However, recording relative changes is still very important in many studies.

1.3.1 Theory

Because the time-averaged rate of absorption must equal the total decay rate (otherwise energy would be piling up in a molecule), we can also express

Eq. (1.2) describing the fluorescence quantum yield Φ_f in terms of intramolecular processes as

$$\Phi_f = k_r/(k_r + k_{nr}), \tag{1.4}$$

where k_r is the radiative decay rate (units s^{-1}), k_{nr} the nonradiative decay rate (composed of internal conversion to the ground state or intersystem crossing to the lowest triplet state), and their sum is the total decay rate. For this reason floppy molecules generally have a lower Φ_f than more rigid molecules. External interactions, for example, collisional quenching by oxygen, bring additional terms to the denominator and further reduce Φ_f. For this reason, oxygen needs to be removed, usually by freeze-pump-thaw cycles or by nitrogen bubbling, for the unquenched Φ_f to be determined correctly. It will be seen that Φ_f can have a maximum value of 1. Unfortunately the simplicity of the definition of Φ_f belies the difficulty of determining it.

1.3.2 Experimental

It can be appreciated from Eq. (1.2) that, in principle, measuring the fluorescence quantum yield requires the determination of the number of photons absorbed and emitted due to fluorescence in a given time. This is a difficult requirement for which integrating spheres can be used. The sample is placed inside a reflective sphere with excitation and emission ports in an attempt to collect all the isotropic fluorescence over a 4π solid angle. Multiple reflections relay the fluorescence to the exit port. Both solids and solutions can be measured. Figure 1.4 shows one such configuration for an integrating sphere. Excitation and fluorescence rays are depicted and re-excitation by one of the fluorescence pathways shown illustrates a common source of error.

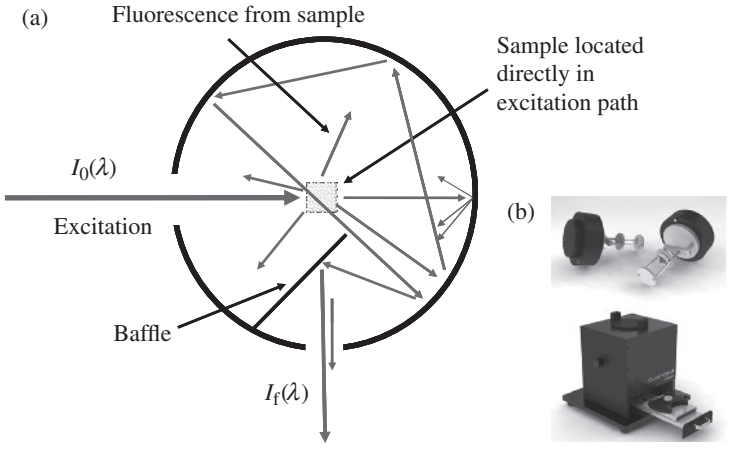

FIGURE 1.4 (a) Typical integrating sphere light paths and (b) construction with sample loading mechanism displayed for cuvettes (top) and solid samples and powders (bottom). Photos courtesy of Horiba Scientific.

A baffle is usually incorporated to minimize reflections from the entrance to exit ports. Excitation light still needs to be spectrally filtered out after the exit port.

Integrating spheres have a long-established [9] and ongoing role to play in the quantification of standards, though they tend to be somewhat impractical and hence not in widespread use. Other absolute methods include calorimetry, photoacoustic spectroscopy actinometry, and thermal lensing. However, the usual recourse is to ratio the spectrally corrected fluorescence spectra of the unknown sample and a suitable reference standard of known quantum yield, that is, to determine a relative rather than an absolute quantum yield. A literature survey soon reveals that fluorescence quantum yields have often courted controversy over the years due to inconsistent measurements between different laboratories. Procedures for absolute and relative quantum yield measurements in solution are discussed in a recent article along with a comprehensive list of references on previous work and recommendations for standards (Table 1.1) [10].

The process by which relative quantum yields are determined involves first correcting the fluorescence spectrum for the spectral responses of the emission monochromator and detecting photomultiplier in order to obtain a true and undistorted fluorescence spectrum. For the sample S and reference standard R, of absorbance A_S and A_R, and respective solvent refractive indices n_S and n_R, we obtain

$$\Phi_{fS} = \frac{\Phi_{fR} I_{fS}(\lambda) A_R n_S^2}{I_{fR}(\lambda) A_S n_R^2}, \tag{1.5}$$

where $I_{fS}(\lambda)$ and $I_{fR}(\lambda)$ refer to the integrated and spectrally corrected fluorescence spectra over wavelength for the sample and reference, respectively. Ideally the same solvent is used for both the sample and reference, but the n^2 ratio corrects for the effect of any solvent difference on the optical geometry over which fluorescence is collected [11]. Solvent refractive index also influences the fluorescence lifetime and the higher precision of lifetime measurement has proved useful in resolving seemingly conflicting results for quantum yield standards [12].

The accuracy in Φ_f is typically no better than 5–10% and such a spread in values is clearly evident in the literature [10]. This seems incongruous with modern day instrumentation, but in fact relative changes of either peak or integrated fluorescence, without measurement of the actual Φ_f, or even spectral correction, are often adequate. The accurate determination of fluorescence quantum yield, like removing the quencher oxygen from solutions before measurement, is no longer of importance in many applications. This is illustrated by the following example.

1.3.3 Application Example—ThT Detection of Sheet Structure

Sheet structures occur in nature, for example, as stacks of graphite and β-sheets of protein or peptide that sometimes form fibrils [13]. Currently sheet structures are of considerable interest when synthesized as isolated monosheets in carbon nanotubes and graphene [14]. Thioflavin T (ThT) is a fluorescent dye (see Fig. 1.5) that has been

TABLE 1.1 Some fluorescence quantum yields (Φ_f) with errors ($\Delta\Phi_f$) at 25°C that can be useful as standards for comparison and determining relative quantum yields

Dye	Quinine sulfate	Coumarin 153	Fluorescein	Rhodamine 6G	Rhodamine 101	Oxazine 1	HITCI	IR125
Solvent	0.105 M $HClO_4$	Ethanol	0.1 M NaOH	Ethanol	Ethanol	Ethanol	Ethanol	DMSO
Absorbance (nm)	270–400	350–500	400–550	425–575	475–620	500–710	535–825	550–875
Emission (nm)	385–700	465–750	490–690	505–750	540–750	615–950	700–950	750–1000
Φ_f	0.59	0.53	0.89	0.91	0.915	0.15	0.30	0.23
$\Delta\Phi_f$	0.04	0.04	0.04	0.04	0.028	0.01	0.01	0.01

Source: Reprinted from Reference 10 with permission of Macmillan Publishers Ltd.

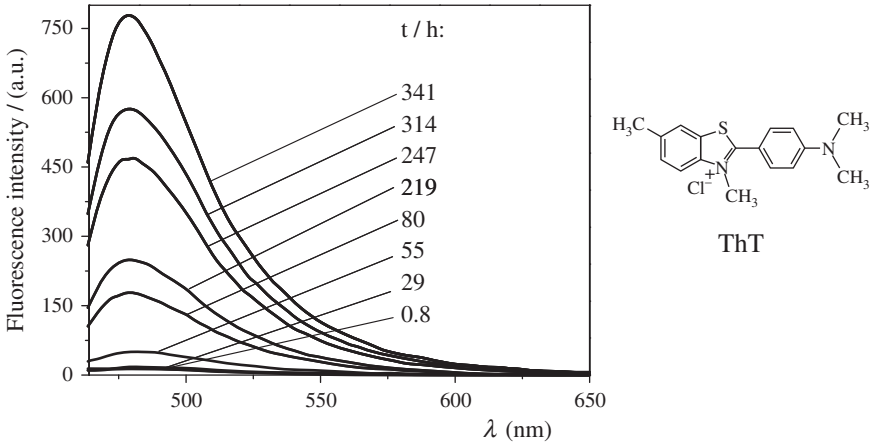

FIGURE 1.5 Increase in ThT fluorescence as beta sheets of Aβ are formed. The excitation wavelength is 450 nm and the fluorescence peak is at 480 nm. Reprinted from Reference 17 with permission from Elsevier.

widely used for revealing the formation of sheet structures [15], most notably when studying the aggregation of the peptide beta-amyloid (Aβ); the early oligomers of which are thought to be the precursor to Alzheimer's disease. As already mentioned, floppy molecules generally have a low fluorescence yield due to having more favorable dissipative pathways other than fluorescence. Conversely rigidity imparts a higher fluorescence yield. ThT behaves as a molecular rotor and upon excitation undergoes intramolecular rotation to a low-fluorescent twisted intramolecular charge transfer (TICT) state [16]. This rotation is restricted between sheet structures, increasing the fluorescence quantum yield, which can thus be used as a probe of sheet formation. Figure 1.5 shows the peak wavelength and shape of the fluorescence spectrum of ThT in Aβ are constant as β-sheets are formed [17]. Hence it is perfectly workable to use the relative change in fluorescence quantum yield to monitor structural changes without actually having to put a number to Φ_f.

One of the limitations of using ThT to detect Aβ aggregation is that the early-stage oligomers, that are thought to disrupt neuronal cellular membranes and initiate Alzheimer's disease, are not detected since only the β-sheets formed later lead to an increase in fluorescence. Changes in fluorescence lifetimes (to be discussed in the next section) have recently been shown to address this short-coming by using the intrinsic tyrosine fluorescence lifetime in the case of Aβ [17] and ThT fluorescence lifetime in the case of insulin fibrils [18].

In cases like eumelanin, where the intrinsic fluorescence is complex (see Fig. 1.3) due to the presence of multiple fluorophores, extrinsic probes with bespoke structural sensing characteristics like ThT come to the fore. Surprisingly, although the composition of melanin is well known to be largely dihydroxyindoles, its secondary structure, the minimum functional unit, and the very existence of a protomolecule

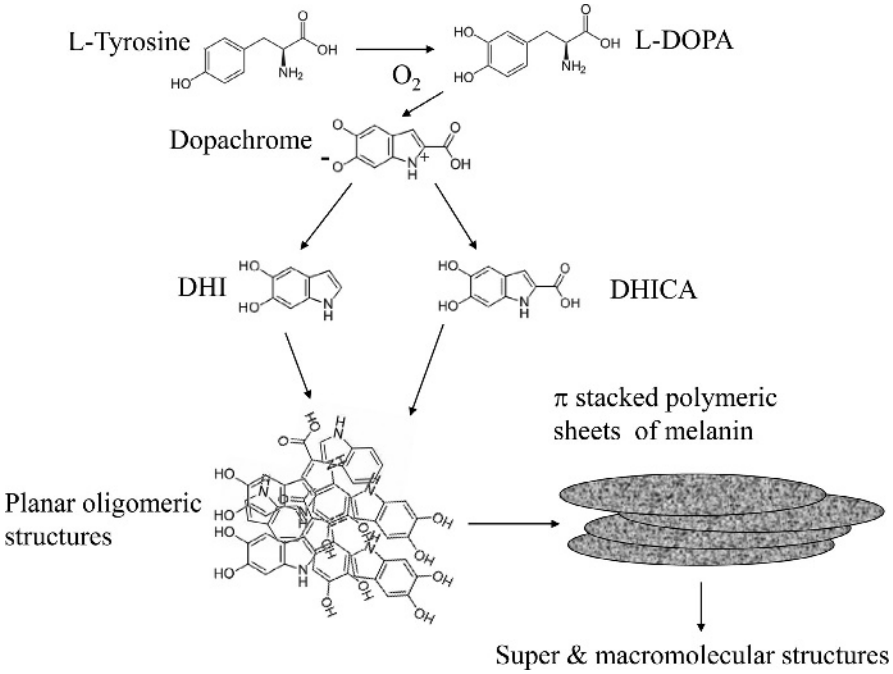

FIGURE 1.6 Probable structural steps in eumelanin synthesis.

that can be replicated to form a secondary structure remains unclear despite decades of research with a whole gamut of techniques [7, 8]. The significance of not knowing the structure of eumelanin has bearing on a whole range of topics from bioelectronics (melanin is an efficient conductor and readily binds metal ions) to melanoma, the most virulent form of skin cancer. The likely structural steps in melanin synthesis are depicted in Figure 1.6.

Planar oligomeric structures of dihydroxyindoles are thought to form sheets that are bound together by π–π interactions. The oxidation of primary structures, either spontaneously or catalyzed, is generally thought to give rise to protomolecules (oligomers) composed of four or five monomers. These combine into planar sheets that stack due to π bonding, albeit less strongly bound than σ covalent bonds, thus accounting for eumelanin's softness in the manner of graphite. The close packing, including π–π^* interactions (∼0.3–0.4 nm apart [8]), being consistent with eumelanin's photo-protection via ultrafast nonradiative relaxation. The larger sheet structures have been proposed to form onion-like layers [19]. Recent fluorescence studies, based on the increase in ThT fluorescence quantum yield as eumelanin is formed by auto-oxidation of L-DOPA, support the notion of assembly via a protomolecule that subsequently forms sheets rather than assembly by monomer addition [20]. This is illustrated in Figure 1.7.

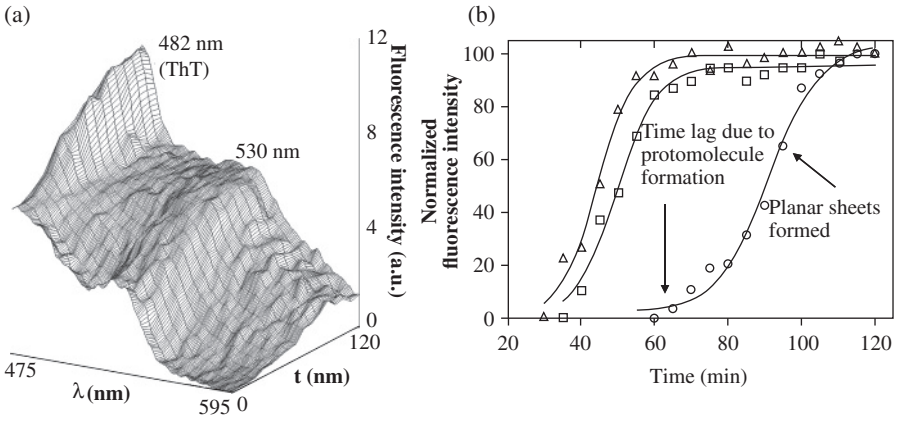

FIGURE 1.7 (a) Fluorescence spectrum of ThT, excited at 450 nm and peaking at 482 nm, superimposed on the intrinsic fluorescence background, as eumelanin is synthesized at pH 10 by the auto-oxidation of L-DOPA. (b) ThT fluorescence at 482 nm as the eumelanin synthesis progresses at pH 10 (∘), pH 10.8 (□) and pH 11.4 (Δ). Reproduced from Reference 20 with permission from AIP Publishing LLC.

The melanin growth, as reflected by the increase in ThT fluorescence can be described using a classic sigmoidal function analogous to that encountered in amyloid fibrillation such as that of Aβ [21]:

$$I_f(t) \sim I_{f0} + I_{max}/\{1 + \exp[-k_m(t - t_{1/2})]\}, \tag{1.6}$$

where $I_f(t)$ is the fluorescence intensity and I_{f0} is the initial or background fluorescence intensity. The parameter I_{max} is the fluorescence maximum above the background, k_m is the rate of melanin formation, and $t_{1/2}$ is the time when the fluorescence intensity has reached the half maximum value.

The very existence of the time-lag suggests that eumelanin is not formed by monomer addition, but rather it requires a protomolecule (or protomolecules) in a "binding ready" conformation to be preformed first. Moreover, the increase in ThT fluorescence in itself further supports the presence of sheet-like structures in eumelanin with the fluorescence no longer increasing when the eumelanin-forming reaction is complete.

1.4 LIFETIME

The fluorescence lifetime of a molecule is the average time it spends in the excited state before emitting a fluorescence photon. Typically in the nanosecond region, the fact that the fluorescence lifetime has a finite value is due to local perturbations and therein rests its usefulness as a probe on the angstrom scale.

Lifetime measurement has emerged in recent years as the most powerful and versatile technique in fluorescence spectroscopy. It can be performed in either the time or frequency domain. In comparison to spectra, quantum yield, and intensity, lifetime provides more kinetic information, a visual image that is easier to interpret, is analogous to a movie compared to a photo, resolves dynamics more closely, provides a more stringent test of kinetics models, and is easier to calibrate. Fluorescence lifetime is also making a mark beyond spectroscopy. For example, in sensing and fluorescence lifetime imaging microscopy (FLIM), to be discussed in Section 1.7.

1.4.1 Theory

The fluorescence lifetime τ_f for aromatic fluorophores can be defined in terms of rate parameters, consistent with the definition for the fluorescence quantum yield Φ_f (Eq. 1.4), as [2]

$$\tau_f = \frac{1}{k_r + k_{nr}}. \tag{1.7}$$

In the time domain, τ_f can be conveniently visualized as it describes the fluorescence impulse response to δ-function excitation at $t = 0$ given by

$$i(t) = i(0)\exp - (t/\tau_f), \tag{1.8}$$

and $i(t)$ is the solution to the rate equation defining the decay of the concentration (population) of the S_1 singlet excited state M^*, due to fluorescence emission:

$$\frac{d\,[M^*]}{dt} = -(k_r + k_{nr})[M^*] = -\frac{[M^*]}{\tau_f} \tag{1.9}$$

if multiple and noninteractive fluorescent emitters are present, the same treatment can be extended linearly by simply adding further exponential terms describing different lifetimes. The application of fluorescence lifetimes has benefitted greatly from the fact that most aromatic fluorophores possess a single exponential decay.

Combining Eqs. (1.4) and (1.7) we obtain

$$\tau_f = \frac{\Phi_f}{k_r}. \tag{1.10}$$

Equation (1.10) illustrates why the fluorescence lifetime can be used to monitor changes that influence fluorescence, as providing the radiative rate k_r remains constant, τ_f offers equivalent information to Φ_f, is easier to measure, more precise and less prone to systematic error. Conversely if Φ_f and τ_f are measured, k_r and k_{nr} can be determined.

k_r can be described by the Einstein coefficient A and the transition dipole moment operator M as [2]

$$k_r = \sum_m Au0 \rightarrow \mathrm{lm} \propto / < \psi_l^* / M / \psi_u > /^2 \tag{1.11}$$

where, unlike for spectral lines in the simpler atomic case, A has to be summed over the whole fluorescence spectrum attributed to the lowest vibrational level u of the excited S_1 singlet state to the different vibrational levels m of the singlet S_0 ground state.

The Strickler–Berg expression [22] and its variants [2] enable k_r to be determined more easily by introducing the Einstein B coefficient relating to the absorption spectrum:

$$k_r = 2.88 \times 10^{-9} n^2 < \upsilon_F^{-3} > A_v^{-1} \int \frac{\varepsilon(\upsilon) d\upsilon}{\upsilon}, \tag{1.12}$$

where $< \upsilon_F^{-3} > A_v^{-1}$ is the reciprocal of the mean value of υ_F^{-3} over the fluorescence spectrum ($\upsilon = 1/\lambda$) and $\int \frac{\varepsilon(\upsilon) d\upsilon}{\upsilon}$ relates to the area under the absorption frequency spectrum.

The fluorescence lifetime dependence on n^2 via the Strickler–Berg equation has been shown to probe refractive index in cells using protein labeled with the green fluorescent protein [23].

Equation (1.12) can be approximated to

$$k_r \sim 10^{-4} / \varepsilon_{max}. \tag{1.13}$$

Given $\varepsilon_{max} \sim 10^5$ mol^{-1} cm^{-1} for a strong absorber, Eq. (1.13) predicts that, in the absence of intramolecular nonradiative processes or intermolecular quenching, τ_f is ~1 ns. It should be cautioned that agreement between Eqs. (1.10) and (1.12) can be quite variable [24] due to potential sources of experimental error (see Section 1.3) and the presence of more complex photophysics, for example, quinine sulfate having a bi- not mono-exponential fluorescence lifetime decay [25]. Significant discrepancies between k_r determined from Eq. (1.10) (which monitors the emitting state) and Eq. (1.12) (which monitors the absorbing state) have often been used to determine the presence of "hidden states," such as those present in polyenes that are facilitated by intra-molecular twisting [26, 27].

In the frequency domain, the equivalent expressions to Eq. (1.8) are

$$\tan \phi = -\omega \tau_f \text{ and} \tag{1.14}$$

$$m = 1/\left(1 + \omega^2 \tau_f^2\right)^{1/2}, \tag{1.15}$$

where ω is the modulation frequency (in rad s^{-1}) and m a modulation factor that describes the relative amplitude of the fluorescence and excitation wave forms. The

negative sign in Eq. (1.14) simply denotes the fluorescence lags the excitation by a phase angle ϕ.

Equations (1.14) and (1.15) lead to an alternative method for measuring fluorescence lifetime as discussed below.

1.4.2 Experimental

There are two main approaches to measuring fluorescence lifetime. Pulse fluorometry in the time domain and phase-modulation fluorometry in the frequency domain [2–4]. The two different approaches are in theory equivalent and complementary, as they are linked by Fourier transforms. For example, δ-function excitation in the time domain is equivalent to exciting with a white frequency spectrum. However, in experimental implementation and data analysis, there are some significant differences that have bearing on the relative merits of the two methods. With phase modulation, the excitation light is modulated or chopped and the fluorescence lifetime determined from either the phase shift or modulation depth of fluorescence with respect to excitation. With pulse fluorometry, a temporally sharp excitation pulse is used and the fluorescence decay recorded with as close a representation of Eq. (1.8) as possible.

Equation (1.14) in particular can be very useful, in so far as it underpins a simple and quick method of determining a single exponential lifetime by measuring ϕ and knowing ω. However, if we think in terms of the equivalence of time and frequency domain measurements the difference is that Eq. (1.14) is a single point (frequency) measurement, whereas Eq. (1.8) offers the prospect of measuring over a wide time range and thus providing a more rigorous test of any kinetic model. This limitation has been ameliorated to some extent by the introduction of various multifrequency methods [3, 28, 29], but at the expense of the simplicity and speed afforded by Eq. (1.14). Despite the advantage of a quick measurement using Eq. (1.14), it would seem pulse fluorometry has found more widespread favor for fluorescence lifetime measurement. The most popular implementation of pulse fluorometry is time-correlated single-photon counting (TCSPC) [30, 31]. Based on delayed coincidence techniques developed for nuclear physics, and then adapted for recording scintillation decay [32], TCSPC and its variants have some critical advantages over other methods, particularly when researching unknown kinetics. The main advantages are

1. Single-photon counting sensitivity down to the single molecule limit such that data precision can be simply enhanced by increasing the measurement time.
2. Temporal display of the kinetics aiding interpretation of data.
3. Known statistical basis (Poisson) and therefore meaningful and objective assessment of the kinetics.
4. As a digital technique it minimizes the effect of signal amplitude variations that can distort analog methods.

Figure 1.8 shows a schematic and photograph of a typical TCSPC fluorometer. The arrangement is very similar to the fluorimeter shown in Figure 1.2, illustrating

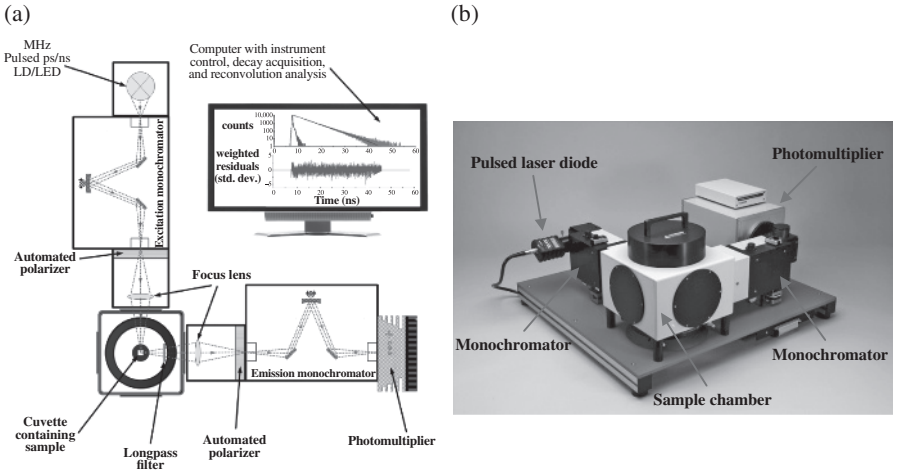

FIGURE 1.8 (a) Schematic of a typical pulse fluorometer and (b) a modular implementation incorporating ps diode laser excitation and microchannel photomultiplier detection. Photo courtesy of Horiba Scientific.

how hybrid instruments can be easily engineered and measurements interchanged simply by swapping components or routing light paths. Polarizers are used primarily for anisotropy decay studies and are not generally needed for lifetime measurements with low viscosity solvents such as water, ethanol, and cyclohexane. However, in viscous solvents, where the fluorophore rotational correlation time is comparable to τ_f, polarizers are used in order to correct for any intrinsic polarization of the fluorometer, such as that caused by diffraction gratings, laser excitation, and so on (see Section 1.6).

These days a semiconductor laser diode (LD) or light-emitting diode (LED) is typically used for excitation. Perhaps surprisingly, a conventional photon counting and timing photomultiplier based on a vacuum tube is still the most widely used detector [33, 34]. Photomultipliers incorporate electron amplification using either discrete or continuous dynodes, the latter incorporated in the microchannel plate photomultiplier, which offers the fastest response. Today semiconductor sources can provide the wavelengths needed to excite most fluorophores. Previously, most pulse fluorometers used the broad spectral continuum of pulsed spark sources [35]. Even though these nanosecond sources were of low repetition rate (∼30 kHz) and low energy (∼10 pJ overall wavelengths), it was still possible to achieve a full spectroscopic capability by using a monochromator rather than a filter on the emission as well as the excitation channel [36]. Semiconductor excitation sources first appeared in TCSPC as red/near-IR AlGaAs diode lasers [37]. The subsequent development of GaN technology [38] provided visible LDs and brought LEDs into the measurement frame [39]. The switch from flashlamps to semiconductor sources was made complete when the critically important area of protein fluorescence was demonstrated using AlGaN LED excitation [40–42]. LED pulse energies are only ∼1 pJ and comparable

to spark sources, but their MHz repetition rates and temporal stability give them clear advantages. TCSPC at repetition rates as high as 100 MHz have been achieved with laser diodes [43]. However, to avoid re-excitation and a "saw tooth" fluorescence decay that is difficult to analyze, this is only practicable for fast lifetimes that fully decay within the 10 ns measurement time window.

Pulse fluorometry measures the photon-time distribution describing the fluorescence decay by using a timing device to measure a "start"–"stop" time interval between excitation of fluorescence and its detection. There are a number of ways to achieve this. These include fast oscilloscopes, sampling oscilloscopes (boxcar integrators), multichannel scaling, stroboscopic detector gating, and a time-to-amplitude converter (TAC), as traditionally used in TCSPC. The TAC converts the time difference t to a voltage v, which is then digitized in an analog to digital convertor and stored as a detected photon count event in a multichannel analyzer (MCA) such that $v \propto t$. Repeating the cycle in accordance with the excitation pulse frequency allows a histogram of counts to be accumulated that is representative of the fluorescence decay, such that D_t is the number of decay counts registered at a time t. Some further refinements and precautions are necessary though.

The pulse height of photomultiplier output for single photon detection is variable due to photoelectrons having different paths and their statistical fluctuation in number. For this reason, and to discriminate against the lower pulse height distribution derived from noise, the timing of photomultiplier signals is derived at a constant fraction of the pulse height (constant fraction discrimination, CFD) [31]. Temporal delays due to optical paths, the photomultiplier, cables, and electronics are inherent, but have no bearing on the quality of measurement, provided they remain constant. A time delay (cable or electronic) that can be varied between measurements to ensure the decay profile is observable and can be moved within the TAC range is essential though. Traditionally nuclear instrument modules (NIMs) were used for the timing electronics, but these have by and large been superseded by customized PC cards or stand-alone modules.

One limitation of the original (simplex) form of TCSPC as described so far is its inefficiency. For the histogram of photon arrival times to reproduce the fluorescence decay curve, the fluorescence detection rate has to be reduced to ∼1% of the source repetition rate in order to avoid data pileup [30, 31]. Otherwise photons arriving early at the peak of the distribution are preferentially recorded and the decay time appears anomalously shortened. This needs a little thought when encountered for the first time, although the 1% ratio also has a statistical basis in that it ensures the probability of detecting two photons per excitation pulse is negligible. Ways of correcting for this inefficiency have long been the focus of attention. Early approaches included statistical analysis [44] and discrimination between one- and multiphoton pulse signals using either photon pulse height or timing [45]. These methods were generally unsatisfactory. In reality, as the repetition rate of sources increased into the MHz range with the advent of mode-locked lasers and semiconductor sources, the 1% count rate was no longer a limitation for cuvette studies and this is still the case today.

However, as the repetition rate of sources increases to the MHz region a second inefficiency of TCSPC emerges; the dead time of the timing electronics when

processing a "stop" signal. This was typically ∼10 μs with traditional TCSPC using a TAC and MCA, thus limiting count rate to ∼100 kHz. This is adequate for many purposes, but much more restrictive than the 1% pile-up limitation when the source repetition rate exceeds 10 MHz. The first step to minimizing the effect of dead time is to simply reverse the "start–stop" roles of the source rate and fluorescence rate, thus reducing the duty cycle of the timing electronics. For the study of transient samples, such as in single-molecule microscopy studies, this is still not good enough. Consequently, faster timing electronics have been developed with such applications in mind that have also become of more general benefit to cuvette-based spectroscopy. At least two orders of magnitude reduction in TCSPC dead time is now common [46], with <10 ns recently reported [43]. Hence measurement times in the millisecond region, with adequate statistics for recording single exponential decay times, are now available.

Another more general limitation of the original simplex form of TCSPC is its inadequacy for accessing much of the multidimensional contour of fluorescence (i.e., intensity, time, polarization, spectra, position) other than through sequential measurements, which can be onerous. For example, time-resolved fluorescence spectra are traditionally measured by sequentially recording the fluorescence decay at different emission wavelengths and then assembling intensity slices at different time delays or recording the whole emission spectrum sequentially at different time delays during the fluorescence decay [3]. The introduction of multiplexed TCSPC [47–49], whereby multiple decay curves are acquired simultaneously, started to address this and continues to be developed using multiple detection channels and timing. Multiplexing techniques are of particular benefit to single-molecule fluorescence microscopy and lifetime imaging [50, 51]. The trend toward miniaturization through lab-on-a-chip developments [52, 53] has facilitated an increase in the number of measurement channels and out-of-the-lab applications [54].

The requirements for data analysis in TCSPC are complicated by the finite duration of the temporal response of the fluorometer. Even if the excitation pulse is effectively a δ-function (i.e., $\ll\tau_f$), the measured fluorescence response will not be identical to the sample's impulse response (e.g., that given by Eq. 1.8). This is largely because of the intrinsic jitter in photoelectron mean transit time in the photomultiplier, to a lesser extent contributed to by the differences in wavelength and optical paths between measuring the excitation and fluorescence. Jitter in the timing electronics, such as the CFD, also contributes, with all these time spreads contributing to the overall instrumental response half-width, approximately as the sum of their squares [31].

The solution is to use convolution analysis, whereby the excitation pulse is considered to be composed of a series of δ-functions and the fluorescence decay a linear superposition of the corresponding fluorescence impulse responses [31] i.e.

$$F(t) = \int_0^t P(t')i(t-t')dt' = P(t) \otimes i\,(t)\,, \tag{1.16}$$

where $F(t)$ is the expected fluorescence decay, which is broader than the fluorescence impulse response $i(t - t')$ because of the effect of the finite instrumental response or prompt $P(t')$. The variable t' is a moving time delay that defines the instant at which each δ-function component of the instrumental pulse generates the start of a fluorescence response, the whole procedure often denoted as $\otimes$ to denote the convolution. $P(t')$ is usually measured by tuning the fluorescence monochromator to the excitation wavelength and replacing the fluorescent sample with a colloid (LUDOX silica [55] is often used) that simulates the isotropic nature of fluorescence by diffuse scattering of the excitation pulse.

Using Eq. (1.16) to analyze fluorescence decay requires numerical analysis using reconvolution rather than deconvolution. That is to say $i(t - t')$ in Eq. (1.16) is iterated to give τ_f from Eq. (1.8) when $F(t)$ best describes the measured decay data D_t, as recorded at channels corresponding to t. Usually nonlinear least squares (NLLS) is the fitting procedure used with a $\chi 2$ goodness-of-fit criterion conveniently providing a single figure of merit for ease of comparison [56]:

$$\chi^2 = \sum_{\substack{\text{Data} \\ \text{channels}}} \left[\frac{D_t - F(t)}{\sqrt{D_t}} \right]^2, \tag{1.17}$$

where $D_t - F(t)$ is the actual deviation (residual) at each datum (squared to allow for the deviations being both positive and negative), $\sqrt{D_t}$ the expected standard deviation, since the statistics are Poisson and for a good fit $\chi^2/(n - \nu) \simeq 1$ for n data channels, and ν the number of parameters to be fitted (decay constants, amplitudes, etc.). In order to interpolate between the temporal widths of the data channels and to provide a first-order correction to the wavelength dependence of the photomultiplier, an additional parameter that shifts $F(t)$ with respect to D_t is usually included.

Other statistical methods are available to further assess the goodness of fit [56]. The weighted residuals, Wt (Eq. 1.18), are also often presented as their distribution underpins χ^2; random rather than systematic deviations being taken to indicate a good fit to the data:

$$W_t = \frac{D_t - F(t)}{\sqrt{D_t}}. \tag{1.18}$$

Figure 1.9 illustrates the foregoing discussion by showing a typical fluorescence decay that is of comparable duration to the excitation pulse and successfully analyzed using reconvolution. Depending on their relative decay times and amplitudes up to three exponential decay components is usually quite straight forward to extract using reconvolution.

While NLLS reconvolution is still the workhorse for decay analysis in TCSPC, other approaches are useful in special cases, for example, the maximum entropy method [57], describing lifetime distributions, and maximum likelihood for handling poor data statistics [58].

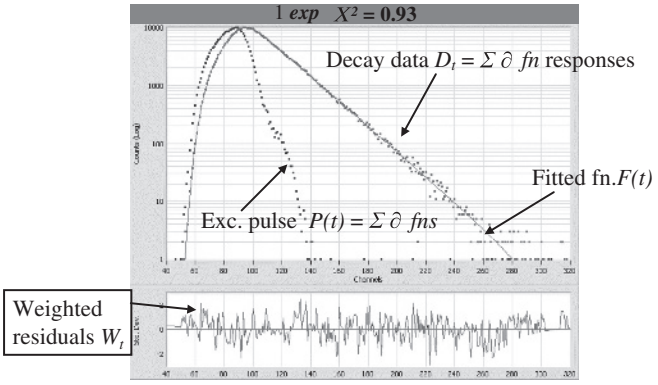

FIGURE 1.9 Reconvolution analysis of a fluorescence decay.

Standards for fluorescence lifetimes have been suggested from a Round-Robin study by nine laboratories that compared results using both pulsed and phase fluorometry for dilute and degassed solutions [59]. Although the idea of chemical standards of time is perhaps in some ways peculiar, they can be quite useful when initially testing fluorometers or in providing confidence in new measurements. Table 1.2 shows some of the average values of up to eight measurements using both TCSPC and phase-modulation measurements taken from this Round-Robin study. Agreement with the TCSPC and phase-modulation results was within a few percent.

1.4.3 Application Example—In Vivo Glucose Sensing

One of the ongoing challenges in biosensing is metabolic monitoring through, and in, the complex barrier of skin and tissue. Monitoring blood glucose for diabetes control is the archetypical measurement problem [60], with the concentration range of physiological interest ~5–30 mM. At present diabetics rely largely on finger-prick blood sampling applied to a reagent strip for glucose analysis, but this has poor patient compliance and is intermittent. Continuous glucose monitors are available that are

TABLE 1.2 Some suggested fluorescence lifetime (τ_f) standards

Dye and solvent	Excitation (nm)	Fluorescence (nm)	τ_f (ns)
Rubrene in methanol	300–514	550–610	9.90 ± 0.30
9,10-Diphenyl anthracene in methanol	295–360	400–475	8.70 ± 0.50
Anthacene in methanol	295–360	375–442	5.10 ± 0.30
2,5-Diphenyloxazole in methanol	295–330	340–400	1.65 ± 0.05
Erythrosin B in methanol	488–568	550–580	0.47 ± 0.02

Source: Adapted from Reference 59 with permission from the American Chemical Society.
Measurements were performed on deoxygenated solutions at 20°C and represent the average of up to eight measurements across different laboratories using both pulsed and phase fluorometry.

based on subcutaneously implanted amperometric enzyme electrodes or microdialysis sensing platforms. Although undoubtedly of benefit and improving, they still have drawbacks that include suboptimal accuracy, drift, and frequent calibration [61]. So far the search for a minimally invasive sensor that can reliably operate continuously has defied advances in modern technology. Many alternative technologies are being investigated, including near-IR, Raman, impedance and photoacoustic spectroscopy, as well as optical coherence tomography, and polarimetry, but none has yet reached routine clinical application [62].

Fluorescence also shows significant promise in this area. It would be ideal if the intrinsic fluorescence of tissue could be used, for example, glucose-induced cellular metabolism of NAD(P)H [63], but the photo-protective action of endogenous absorbers such as melanin makes this impractical. Extrinsic fluorescence platforms include those based on boronic acid [64], concanavalin A [65], carbon nanotubes [66] and enzymes, such as hexokinase [67], and glucose/galactose binding protein [68]. Each of these assays has strength and weakness, but ultimately a workable assay will need to operate in the red/near-IR therapeutic spectral window in order to minimize absorption and scattering by endogenous species. However, some such sensing schemes have been reported [66,69,70].

The advantages of fluorescence lifetime over intensity measurements come to the fore in applications like glucose sensing. Fluorescence lifetimes are essentially independent of fluorophore concentration, photobleaching, and ground-state quenching, they can discriminate against scattered excitation light and auto-fluorescence, and are easy to calibrate absolutely. Moreover, recent developments in semiconductor photonics and on-chip integration, some are already mentioned, combined with fiber optics, mean that ergonomic and miniaturized instrument systems, using either pulse or phase fluorometry, are well within reach for glucose sensing.

By way of an example, here we describe a reversible fluorescence lifetime platform based on glucose/galactose-binding protein (GBP) from *Escherichia coli*. GBP has a single polypeptide chain that folds into two lobular domains, separated by a hinge region where glucose binds (Fig. 1.10). Binding is accompanied by a marked conformational change in the protein, with the two lobules closing round the glucose molecule to form a "closed-form" of GBP. When appropriately labeled, the glucose-induced conformational change in GBP can produce a significant change in fluorescence [71]. In Figure 1.10 the environmentally sensitive probe badan (6-bromoacetyl-2-dimethylaminonaphthalene) is attached to position H152C (i.e., a mutant where histidine is substituted by cysteine at position 152 of the polypeptide chain near the glucose-binding site). The addition of glucose results in a 300% increase in fluorescence intensity [71]. In the presence of glucose the fluorescence decay can be described well by an impulse response comprising two time constants of $\tau_{f1} \sim 1$ ns and $\tau_{f2} \sim 3$ ns. These components are associated with an equilibrium that depends on the glucose concentration between the open (and quenched) glucose-free and closed (and enhanced) glucose-bound forms of GBP, respectively. The fluorescence impulse response, with reference to Eq. (1.8), is

$$i(t) = i_1 \exp -(t/\tau_{\mathrm{f1}}) + i_2 \exp -(t/\tau_{\mathrm{f2}}). \tag{1.19}$$

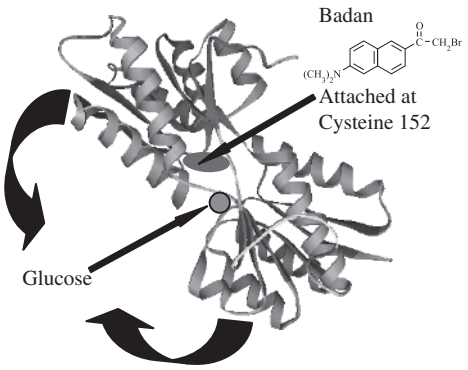

FIGURE 1.10 Glucose/galactose-binding protein (GBP), genetically modified and labeled with badan [71]. When glucose enters the cleft, the hinged lobes fold together, increasing the fluorescence of the badan label.

Figure 1.11a shows the relative change in fluorescence fractions F_1 and F_2 as the glucose concentration is varied in neutral buffer to include the 5–30 mM physiological range. This is in terms of the weighted average $<\tau_f>$ for the two decay components:

$$< \tau_f >= \frac{i_1\tau_{f1}}{i_1\tau_{f1} + i_2\tau_{f2}}\tau_{f1} + \frac{i_2\tau_{f2}}{i_1\tau_{f1} + i_2\tau_{f2}}\tau_{f2} = F_1\tau_{f1} + F_2\tau_{f2}. \qquad (1.20)$$

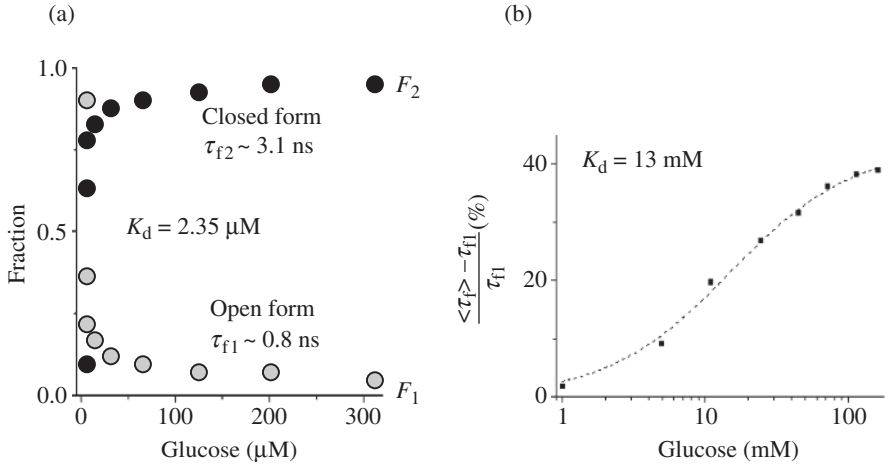

FIGURE 1.11 (a) Fractions of fluorescence due to open, F_1, and closed, F_2, forms of GBP-badan with $K_d = 2.35$ μM in PBS buffer at pH 7.4. (b) Percentage change in average lifetime $\frac{<\tau_f>-\tau_{f1}}{\tau_{f1}}$ (cf. Eq. 1.20) as a function of glucose concentration for a GBP mutant, immobilized on agarose beads coupled to an optical fiber in PBS buffer at pH 7.4, with K_d of 13 mM designed for the physiological range [72].

Figure 1.11b was obtained for badan-GBP immobilized on agarose beads coupled to an optical fiber in neutral buffer, an approach which could also be suitable for implanting in subcutaneous tissue [72]. The dissociation constant K_d is 13 mM and ideal for monitoring over the physiological range of glucose. The measurand is the fractional increase in $<\tau_f>$ on addition of glucose as compared to the fluorescence lifetime at zero glucose τ_{f1}.

GBP labeled with acrylodan (a similar dye to badan) has recently been successfully demonstrated in preclinical trials on swine using a fiber optic insert in the subcutaneous tissue and found to be free from significant effects of common interferents [73]. Badan-GBP has also been encapsulated on a micron scale in layer-by-layer assemblies of poly-lysine and poly-glutamic acid and demonstrated in plasma, paving the way to a minimally invasive implementation as a smart tattoo [74].

The underlying mechanism behind the large increase in badan-GBP fluorescence when glucose binds, and GBP folds, is likely to be complex. Badan is well known to be environmentally sensitive with a fluorescence spectrum that shifts with solvent polarity; however, in this case the fluorescence spectrum shows little change. Some of the more commonly encountered fluorescence quenching mechanisms are discussed in the next section.

1.5 QUENCHING

A fluorescence quencher can be simply defined as any species, which, by interacting with the fluorophore, reduces its quantum yield. There are many molecular mechanisms of quenching, each lowering the proportion of the number of radiative transitions in respect to the number of photons absorbed (Eq. 1.4).

Quenching studies are useful in gaining information on accessibility to the quencher, determining location of fluorophores, diffusion parameters, and permeability and structure of media and macromolecules. They have also led to a whole range of sensors for detecting different analytes. The primary experimental techniques for studying quenching have already been described, namely spectra (both absorption and fluorescence), quantum yield, and lifetime. Again the latter is better placed to reveal most about the quenching kinetics and bring to bear advantages in sensing already mentioned for the case of glucose monitoring. In all fluorescence quenching studies it needs to be kept in mind that a single quenching mechanism is not always present and often more complicated hybrid kinetics are observed. Here we summarize the most commonly encountered forms of fluorescence quenching.

1.5.1 Theory

1.5.1.1 Static Quenching Perhaps the most trivial form of quenching is so-called static quenching where the quencher molecules Q form ground-state complexes with the fluorophore M (Fig. 1.12a). The MQ complexes can still be excited, but either do not fluoresce or have a reduced fluorescence quantum yield.

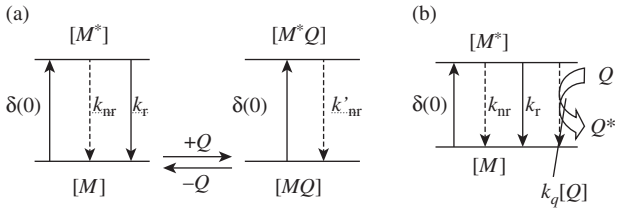

FIGURE 1.12 (a) Schematics of the mechanism of static quenching. The MQ complex can be excited, but is not fluorescent. As Q does not affect the M excited state, there is no change in its fluorescence lifetime. (b) Dynamic quenching.

The association constant, K_s, controls the equilibrium between free and fluorophore–quencher complexes:

$$K_s = \frac{[MQ]}{[M]_q[Q]} = \frac{[M]_0 - [M]_q}{[M]_q[Q]}, \tag{1.21}$$

where $[M]_q$, $[Q]$, and $[MQ]$ are the concentrations of the ground state molecular fluorophore, quencher, and fluorophore–quencher complex, respectively, in the presence of the quencher. $[M]_0$ is the initial concentration of the fluorophore in the absence of the quencher and $[M]_q$ the concentration of the fluorophore in the presence of the quencher. Equation (1.21) can be easily converted into the well-known Stern–Volmer equation [3]:

$$\frac{I_f}{I_{fq}} = \frac{[M]_0}{[M]_q} = 1 + K_s[Q], \tag{1.22}$$

where I_f and I_{fq} are the fluorescence intensities measured in the absence and presence of the quencher, respectively. The absorption spectrum can reveal evidence for the presence of static quenching as MQ will be likely to have a different spectrum to M. However, because static quenching does not interfere with the excited-state kinetics, but only reduces the concentration of the fluorescent dye, no change in fluorescence lifetime is observed. In addition to well-known static quenchers, for example, mercury ions, some newly developed materials, such as graphene [75] and carbon nanotubes [76], have also been recently found to act as static quenchers for certain dyes.

1.5.1.2 Dynamic Quenching Dynamic quenching occurs during the collision of the electronically excited molecule M^* and the quenching molecule Q (see Fig. 1.12b). During the collision, the excitation energy is transferred to the quencher and dissipated as heat. Because the excited state kinetics is affected, the fluorescence lifetime in addition to the yield is reduced.

The kinetic equations for the concentration of the excited dye $[M^*]$, following δ-function excitation at $t = 0$, in the absence and in the presence of a quencher Q, are given by Eq. (1.9) and Eq. (1.23), respectively.

$$[Q] > 0 \;\Rightarrow\; \frac{d[M^*]}{dt} = -(\tau_{\mathrm{f}}^{-1} + k_{\mathrm{q}}[Q])[M^*], \tag{1.23}$$

where τ_{f} is the fluorescence lifetime in the absence of quencher and k_{q} is the diffusion-controlled quenching rate constant. In the steady state $d[M^*]/dt = 0$. These equations yield the Stern–Volmer equation for dynamic quenching and fluorescence intensities analogous to static quenching, but this time including the lifetime:

$$\frac{I_{\mathrm{f}}}{I_{\mathrm{fq}}} = \frac{\tau_{\mathrm{f}}^{-1} + k_{\mathrm{q}}\,[Q]}{\tau_{\mathrm{f}}^{-1}} = 1 + \tau_{\mathrm{f}} k_{\mathrm{q}}\,[Q]\,. \tag{1.24}$$

The solution of Eq. (1.23) (equivalent to Eq. (1.8), but including quenching) is $[M^*] = [M^*]_0 \exp(-t/\tau_{\mathrm{fq}})$, where

$$\frac{1}{\tau_{\mathrm{fq}}} = \frac{1}{\tau_{\mathrm{f}}} + k_{\mathrm{q}}\,[Q]\,. \tag{1.25}$$

This indicates that the fluorescence decay of the dynamically quenched dye remains exponential, but with a reduced lifetime $\tau_{\mathrm{fq}} < \tau_{\mathrm{f}}$. After simple rearrangement of Eq. (1.25), we obtain the Stern–Volmer dependence for lifetimes:

$$\frac{\tau_{\mathrm{f}}}{\tau_{\mathrm{fq}}} = 1 + \tau_{\mathrm{f}} k_{\mathrm{q}}\,[Q]\,. \tag{1.26}$$

The right-hand side of this equation is the same as in Eq. (1.24) with both steady-state and time-resolved fluorescence yielding the Stern–Volmer constant $K_{\mathrm{SV}} = \tau_{\mathrm{f}} k_{\mathrm{q}}$ of dimension M^{-1}.

Several compounds, often containing heavy atoms to facilitate intersystem crossing to the triplet state, are well known as dynamic quenching agents when present at sufficiently high concentration. This has led to a wide range of structural probes and analyte sensors based on the Stern–Volmer equation. For example, oxygen, with a triplet ground state and occurring at $\sim 10^{-3}$ M in aliphatic solvents, is a highly efficient dynamic quencher of fluorescence (diffusion constant in water $\sim 10^{-5}$ cm^2 s^{-1}). Oxygen sensors based on the long-lived excited states of transition metal complexes have been extensively developed [77,78]. Other quenchers include chloride, bromide, and iodide ions [79, 80]; transition, noble, and heavy metals [81, 82]; amines; carbon tetrachloride; and acrylamide [83, 84].

In some cases, collisional interactions can result in the formation of an excimer or exciplex [2] which have their own fluorescence characteristics and add complexity to the kinetics. Indeed carbon tetrahalides have been shown to exhibit hybrid quenching composed of static, dynamic, and exciplex components [2].

In addition, k_q is not always a constant, but has a $\sqrt{t}$ time dependence that in the simplest case can be derived from Smoluchowski's solution [85] of the diffusion equation

$$k_q = 4\pi RD\left[1 + \frac{R}{\sqrt{\pi Dt}}\right], \tag{1.27}$$

where D is the sum of the diffusion coefficients of the fluorophore and quencher and R is the sum of their interaction radii.

This leads to a nonexponential impulse response given by [3]

$$i(t) = i_0 \exp\left[-t/\tau_{fq} - 2b\left(t/\tau_{fq}\right)^{1/2}\right], \tag{1.28}$$

where $b = 4R^2 N_A(\pi D)^{\frac{1}{2}}\ [Q]/1000$ and N_A = Avogadro's number.

Such transient effects are exaggerated in higher viscosity solvents such as glycerol, which reduces collisional quenching, but can be observed even in low viscosity solvents such as ethanol at higher time resolution. It can be observed as a departure from an exponential decay at short times in both TCSPC and phase fluorometry, with and without excimer/exciplex formation [86–88].

1.5.1.3 Förster Resonance Energy Transfer Direct collisional contact between the dye and the quencher is not required in the third common mechanism of quenching that we will consider. Förster resonance energy transfer (FRET) has become popular in recent years as a "spectroscopic ruler" for measuring distances and studying the structure and dynamics of macromolecular and microheterogeneous molecular systems [89]. Named after Theodor Förster, who discovered and described the quantum-mechanical nature of this phenomenon in the late 1940s, the mathematical description of FRET is obtained by applying perturbation methods to an excited dye–quencher pair, which are denoted donor D and acceptor A (see Fig. 1.13). The interaction is usually dipole–dipole in origin, and the spectral overlap (the "resonance") between the donor fluorescence and acceptor absorption is a prerequisite for FRET and this gives it higher intrinsic specificity than collisional quenching.

Förster's treatment gives the rate of D–A energy transfer k_{DA} to be

$$k_{DA} = \frac{1}{\tau_D}\left(\frac{R_0}{r}\right)^6, \tag{1.29}$$

where r is the D–A distance (both D and A are regarded as point dipoles and thus assumed to have no spatial dimension) and τ_D is the fluorescence lifetime of the donor in the absence of acceptor (τ_f as defined previously). Since the k_{DA} is proportional to the inverse sixth power of the distance r, FRET can be used as an extremely sensitive mechanism for determining D–A separations and thus measuring molecular distances. The actual scale of this "molecular ruler" is determined by the parameter

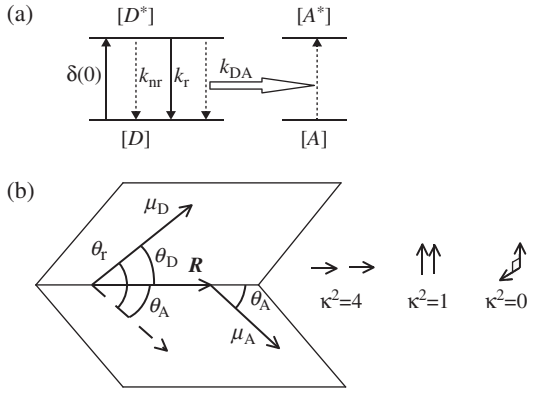

FIGURE 1.13 (a) The mechanism of Förster resonance energy transfer. (b) The orientation factor in FRET. μ_D and μ_A are the transition dipole moments of donor and acceptor molecules and R is the separation vector.

R_0, the Förster or critical transfer distance. According to Förster's theory, R_0 can be calculated using the relevant spectroscopic properties of the donor and acceptor:

$$R_0^6 = \frac{9000 \ln(10) \kappa^2 \Phi_f}{128 \pi^5 N_A n^4} \int_0^\infty I_D(\lambda) \varepsilon_A(\lambda) \lambda^4 d\lambda, \tag{1.30}$$

where κ^2 is the orientational factor, Φ_f the quantum yield of donor fluorescence (without acceptor), N_A the Avogadro's number, and n the refractive index of the intervening medium. The integral in Eq. (1.30) represents the degree of spectral overlap between the donor fluorescence spectrum $I_D(\lambda)$ and the acceptor absorption spectrum $\varepsilon_A(\lambda)$. Significant spectral overlap ensures a high critical transfer distance R_0 (typical values vary from ∼10 to 100 Å) and thus a high rate of FRET. Equation (1.29) allows the determination of D–A separations; this simple equation finds numerous applications in the materials and life sciences. The other critical factor affecting R_0 is the orientational factor κ^2, defined as

$$\kappa^2 = [\cos \theta_T - 3 \cos \theta_D \cos \theta_A]^2. \tag{1.31}$$

The angles are defined in Figure 1.13b, where some limiting situations have also been depicted for $0 < \kappa^2 < 4$.

For fast and freely rotating donor and acceptor molecules, κ^2 can be averaged over time and equals 0.67 and this assumption often has to be made even when not strictly correct. If the mutual orientation of D and A is not fully random, the orientational effects may significantly affect FRET, which can be explored to extract extra structural information. The orientational dependence of FRET has been discussed in numerous studies [90] and recently conclusively demonstrated using labeled nucleic acids [91].

The presence of FRET is manifest in the fluorescence spectrum of the sample by a decrease in the intensity of the donor spectrum and increase in the acceptor spectrum (if the acceptor is fluorescent). FRET not only reduces the intensity of donor fluorescence but also affects its fluorescence decay. In the simplest case, if the original donor decay is a single exponential with the lifetime τ_D and D and A are separated at the fixed distance r_{DA}, then the fluorescence impulse response is

$$i(t) = i_0 \exp\left[-\left(1 + \left(\frac{R_0}{r_{DA}}\right)^6\right)\frac{t}{\tau_D}\right]. \tag{1.32}$$

Equation (1.32) shows that the decay remains a single exponential, but with a reduced lifetime that allows determination of the D–A distance.

In the presence of acceptors distributed around the donors according to the D–A distribution function $\rho(r)$, the fluorescence impulse response is modified to

$$i(t) = i_0 \exp[-t/\tau_D - \int_0^\infty \left(1 - tk_{DA}(r)\right)\rho(r)\,dr]. \tag{1.33}$$

Equation (1.33) shows the potential of FRET for not only determining distances but also studying the morphology of a medium on the sub-nanometer scale. Unfortunately, although initially promising, without making *a priori* assumptions, interpretation of FRET in amorphous materials such as silica was found to be limited to fractals and simple model geometries [92, 93] and not give the detailed morphology sought. The underlying problem is the ill-posed nature of Eq. (1.33), such that a unique solution for the distribution function $\rho(r)$ does not usually exist. The usual approach is to assume a hypothetical formula for $\rho(r)$ and then try to determine the "best-fit" parameters.

Fortunately Eq. (1.33) can be solved for the most commonly encountered special case, namely that of a random distribution of acceptors $\rho(r) \sim r^2$, leading to the well-known Förster decay function

$$i(t) = i_0 \exp[-t/\tau_D - \gamma\left(t/\tau_D\right)^{1/2}], \tag{1.34}$$

where $\gamma = [A]/C_A$, and

$$C_A = \frac{3}{4\pi^{3/2}R_0^3 N_A}, \tag{1.35}$$

where $[A]$ is the actual acceptor concentration and C_A the critical molar acceptor concentration.

Equation (1.34) can be implemented in different ways. For example R_0 can be determined from Eq. (1.30) to give C_A using Eq. (1.35). Then by reconvoluting Eq. (1.34) in order to fit to the experimental fluorescence decay, the local concentration of the acceptor in the donor environment can be found. In microheterogeneous

systems, this may well not be the same as the bulk concentration, thus indicating structure, accessibility, or other information from the donor–acceptor proximity. The measurement is effectively the same when FRET is used as a sensor platform for determining the presence and concentration of analytes of interest and we illustrate this in the next section.

1.5.2 Application—Metal Ion Quenching

Metal ion detection has widespread relevance to many important areas that include human metabolism, neurology, and the environment. By way of an example of fluorescence-based sensing, we consider here the quenching by copper ions in different media of the red/near-IR fluorescent dye carbocyanine dye, 3,3-diethylthiadicarbocyanine iodide (DTDCI). Hydrated copper ions ($Cu^{2+}{\cdot}5H_2O$) can quench both collisionally and by FRET via an overlapping broad band absorption that peaks around 800 nm.

Figure 1.14 presents the result of fitting Eq. (1.34) to the fluorescence decay for DTDCI quenched by hydrated copper ions in propylene glycol (a and b), and in water pools (c and d) of a hydrated perfluorosulfonate ion exchange membrane (Nafion, Dupont Corp.) [94]. Plots a and b show a "pure" FRET example that is described by Eq. (1.34), that is, a constant value of the donor lifetime τ_D and γ increasing linearly with copper ion concentration. Plots c and d show an example of a not infrequent case of hybrid kinetics where FRET is accompanied by collisional quenching, which leads to a decrease of the donor lifetime with increasing quencher concentration.

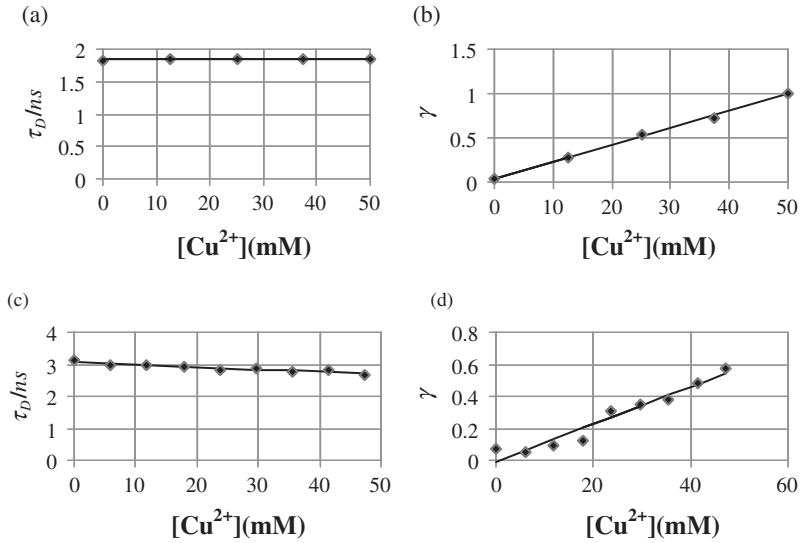

FIGURE 1.14 Donor lifetimes τ_D and γ values for the DTDCI→Cu^{2+} quenching in propylene glycol (a and b), and in Nafion (c and d) [94].

Notwithstanding the homogeneous and heterogeneous differences in the two media, the dominant difference between the two cases is the much lower diffusion coefficient ($\sim 10^{-7}$ cm^2 s^{-1}) in propylene glycol. Such behavior has been observed in numerous other combinations, for example, Cu^{2+} sensing down to 10 ppb in Nafion using rhodamine 800 as a donor [95]. Models of increasing complexity have been proposed for handling such hybrid kinetics, starting with essentially linear combinations of collisional and FRET terms [96].

Two of the advantages of using hydrated transition metal ions as acceptors are their good approximation to the point dipole demanded by Förster's theory and minimal disturbance of native structure. These have been recently put to good effect when measuring distances in model α-helical peptides [97, 98]. However, transition metal ion acceptors have the disadvantage of a relatively short R_0 value ($\sim$1–2 nm) caused by the weak d–d transitions as compared to the π–π^* transitions of aromatic acceptors. This problem can be overcome in sensing by using a chelating molecule, for example, bathocuproine used for Cu(I) [99]. For FRET sensing of the colorless metal ion zinc, a fluorescently labeled enzyme, carbonic anhydrase II, has been successfully used [100, 101]. Quantum dots are emerging as a more robust donor than aromatic dyes for sensing metal ions, although their decay time kinetics can also be complex [102]. Although comparatively large in size ($\sim$2–6 nm) [103], they are still a useful alternative to conventional dyes when bound to protein for FRET studies [104]. Similarly green fluorescent protein [105] and its subsequent other visible forms are finding increasing use with FRET [106].

1.6 ANISOTROPY

Fluorescence anisotropy describes the polarization of fluorescence and along with quenching, is one of the most important methods in fluorescence spectroscopy, particularly when time-resolved using similar techniques to those already described for the measurement of fluorescence lifetimes. Just as fluorescence quenching is influenced by translational diffusion or proximity for FRET to occur, fluorescence anisotropy is influenced by rotational diffusion and energy migration. The importance of FRET and anisotropy can be judged from their sub-nanometer spatial resolution, which is over an order of magnitude better than any techniques using an optical microscope. This has led to their application as a tool for molecular nanometrology.

1.6.1 Theory

The basis of fluorescence anisotropy techniques is to use polarized excitation to create a spatially selected, non-random, distribution of excited fluorescent molecules which then randomize, most commonly by Brownian rotation, but also at times by energy migration depending on the system. The extent by which the fluorescence emission is depolarized depends on the rotation of the fluorophore (or extent of energy migration or both), which in turn brings with it the measurement of parameters that influence molecular rotation. Figure 1.15 shows a typical geometrical arrangement with respect

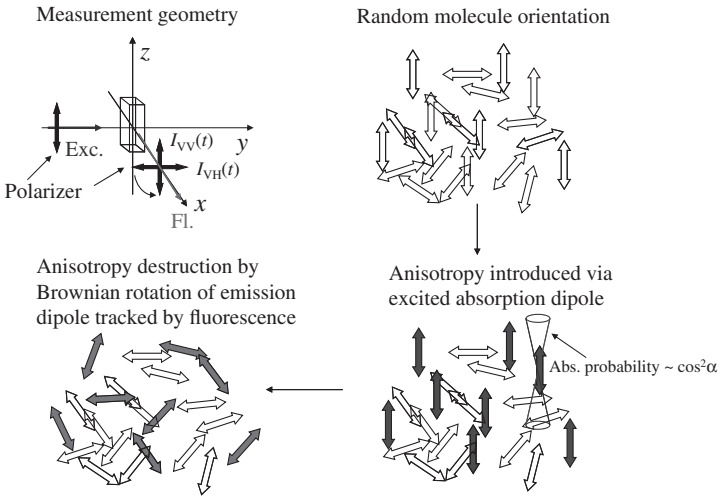

FIGURE 1.15 Measurement geometry for anisotropy studies, selective excitation using polarized light and depolarized fluorescence emission due to Brownian rotation. The probability of excitation goes as $\cos^2\alpha$, where α is the angle between the plane of polarization and the absorption dipole.

to the spectrometers shown in Figures 1.2 and 1.8 and the photoselection in a random distribution of molecules that is designed to be produced. Both steady-state and time-resolved anisotropy can be performed using the configuration shown in Figure 1.15.

The theory of fluorescence anisotropy has developed over many years from the work of Perrin, Jablonski, Weber, Wahl, and others [3] and has been frequently reviewed [107, 108].

Both steady-state and time-resolved anisotropy can be measured using the configuration of Figure 1.15. By recording vertically (V) and horizontally (H) polarized fluorescence decay curves, $I_{VV}(t)$ and $I_{VH}(t)$, orthogonal to vertically (V) polarized excitation, a time-resolved anisotropy function $r(t)$ can be generated that is much more revealing (particularly if heterogeneous depolarization mechanisms are present) than the steady-state anisotropy, that provides just a time average, as it neglects the time dependence, that is,

$$r(t) = \frac{I_{VV}(t) - GI_{VH}(t)}{I_{VV}(t) + 2GI_{VH}(t)}, \tag{1.36}$$

where G is a factor ($G = I_{HV}(t)/I_{HH}(t)$) determined for horizontal orientation of the excitation polarizer in order to correct for differences in the polarization transmissions of the fluorescence detection channel at V and H, which are largely due to the emission monochromator. The factor of 2 in the denominator arises because there is a plane in the direction of the excitation in which depolarization of fluorescence is not detected, but which is identical to that detected in the emission channel. Because

the denominator in Eq. (1.36) describes all three planes of polarization, it actually also describes the fluorescence decay undistorted by any polarization bias. This can be seen from inserting Eqs. (1.37) and (1.38) below into Eq. (1.36) for the simplest depolarization case where a fluorophore can be treated as a spherical rigid rotor undergoing Brownian isotropic rotation in a medium such as a solvent for

$$I_{VV}(t) = \exp(-t/\tau_f)[1 + 2r_0 \exp(-t/\tau_c)], \tag{1.37}$$

$$I_{VH}(t) = \exp(-t/\tau_f)[1 - r_0 \exp(-t/\tau_c)], \tag{1.38}$$

whereby we obtain

$$r(t) = r_0 \exp\left(-\frac{t}{\tau_c}\right), \tag{1.39}$$

where r_0 is the initial anisotropy at $t = 0$, which has a maximum value of 0.4 for one photon excitation, and τ_c the rotational correlation time, which describes the rate of depolarization due to isotropic rotation.

In this case, τ_c can be described by the Stokes–Einstein equation:

$$\tau_c = \frac{\eta V}{kT} = \frac{1}{6D}, \tag{1.40}$$

where η is the microviscosity, V the hydrodynamic volume $= 4\pi R^3/3$ prescribed by the rotor of hydrodynamic radius R, T the temperature, k the Boltzmann constant, and D the rotational diffusion coefficient.

The denominator in Eq. (1.36) can be useful in determining τ_f free from errors due to polarization effects when τ_f is comparable to the rotational correlation time τ_c, such as might occur for aromatic fluorophores in viscous solvents. An alternative adaptation of Figure 1.15 achieves the same by having vertical excitation polarization and the emission polarizer at the so-called magic angle of 54.8° to the vertical. The same aim can also be achieved at other specific polarizer orientations [30].

In the case where a fluorophore is partitioned between two different environments characterized by τ_{c1} and τ_{c2} or has a bimodal anisotropic rotation [109], then providing τ_f is the same for each rotational component:

$$r(t) = (1 - f)r_0 \exp\left(-\frac{t}{\tau_{c1}}\right) + fr_0 \exp\left(-\frac{t}{\tau_{c2}}\right), \tag{1.41}$$

where f defines the fraction of fluorescence associated with each decay component.

Equation (1.41) finds wide-ranging application, including that of nanoparticle metrology in the example given in Section 1.6.3 [110].

If the fluorophore undergoes restricted motion such as in a lipid bilayer [111], or wobbles when tethered to a slowly rotating macromolecule such as a protein [107], then Eq. (1.41) is modified for these special cases, since $\tau_{c2} \gg \tau_{c1}$, to give

$$r(t) = (1 - f)r_0 \exp\left(-\frac{t}{\tau_{c1}}\right) + fr_0\,, \tag{1.42}$$

fr_0 is sometimes referred to as the residual anisotropy r_∞ and in the case of lipid bilayer membranes leads to the determination of an order parameter S for the membrane from [111]

$$S = \sqrt{\frac{r_\infty}{r_0}}. \tag{1.43}$$

Although often an approximation sometimes Eqs. (1.41) and (1.42) can be combined to useful effect to give

$$r(t) = (1 - f - g)r_0 \exp\left(-\frac{t}{\tau_{c1}}\right) + fr_0 \exp\left(-\frac{t}{\tau_{c2}}\right) + gr_0 \tag{1.44}$$

For example, Eq. (1.44) is useful where unbound dye coexists alongside dye wobbling when bound to a slowly rotating nanoparticle.

1.6.2 Experimental

The experimental methodologies for steady-state and time-resolved anisotropy measurements are achieved by combining the techniques described in Sections 1.2 and 1.4, respectively, with the polarization orientations shown in Figure 1.15. One extra point of care is to ensure that in determining fluorescence anisotropy from Eq. (1.36) any fluctuations in the source intensity are corrected. This is usually achieved by averaging out any drift by alternating between the measurement of $I_{VV}(t)$ and $I_{VH}(t)$, and sometimes by the use of a T-format, which offers continuous correction [48].

Although there are different approaches to the analysis of anisotropy decay data, the usual method is to use NLLS in an analogous manner to that described in Section 1.4.2 for fluorescence lifetime analysis. Rearranging the anisotropy function given by Eq. (1.36), we obtain

$$d_t = r(t)[I_{VV}(t) + 2GI_{VH}(t)] = I_{VV}(t) - GI_{VH}(t). \tag{1.45}$$

The function within square brackets in Eq. (1.45) is the fluorescence decay, which we can fit to separately using as many decay parameters as required to give a good fit in order to obtain the fluorescence impulse response $i(t)$ and then keep it fixed, that is, with reference to Eq. (1.19) i_1, τ_{f1}, i_2, τ_{f2}, and so on. The function on the right-hand side of Eq. (1.45) contains the difference data d_t that carries the rotational information and which we can iteratively fit to using NLLS reconvolution of $P(t)$ with

anisotropy impulse response functions $r(t)$ that are intuitively thought to be applicable (e.g., Eq. 1.39, 1.41, or 1.44). Then, we obtain r_0, τ_{c1}, and τ_{c2}, again using χ^2 as the goodness-of-fit criterion, that is,

$$\chi^2 = \sum_{\substack{\text{Data} \\ \text{channels}}} \left[\frac{d_t - P(t) \otimes r(t) i(t)}{\sqrt{d_t}} \right]^2 \tag{1.46}$$

Since the rotation is tracked by the fluorescence decay, ideally τ_c should be $\sim\tau_f$.

In comparison to fluorescence quantum yield and lifetime, there are not really any established standards for rotational correlation time. The rotation of rhodamine 6G has perhaps been studied the most and is probably the nearest to a standard. Some rotational measurements on rhodamine 6G are listed in Table 1.3. The effect of solvent in sticking to rotating fluorophores needs to be kept in mind when considering fluorescence anisotropy [108].

The advantages of using rhodamine 6G as a standard are that it is an isotropic rotor, has a monoexponential fluorescence decay ($\tau_f \sim 4$ ns [115, 116]) and a high fluorescence quantum yield (0.91 in ethanol [10]), is commercially available in high purity, and is photo- and chemically stable over a wide range of pH (<2 to >12). Other xanthene dyes, for example, rhodamine 101, have also been considered as rotational standards, and a useful IUPAC Technical Report [117] recently listed rotational data on a range of fluorophores, including rhodamine 6G and rhodamine 101, and made recommendations for checking the accuracy of measurements. It should be noted however that r_0 for rhodamine 6G decreases quite rapidly when excited below its 0-0 transition, which is ~515 nm [117].

TABLE 1.3 Some reported rotational parameters for rhodamine 6G using one-photon excitation and a range of techniques

Hydrodynamic radius R (Å)	Temperature (°C)	Excitation (nm)	τ_c (ps) in ethanol	τ_c (ps) in methanol	τ_c (ns) in propylene glycol
6.0 ± 0.03 [112]					
5.4 [113]	Not specified. Probably room temperature	530	175 ± 13	91 ± 8	
5.4 [114]	21	580	195 ± 5	95 ± 3	
5.6 ± 0.1 [115]					
5.3 ± 0.3 [116]					
	27	400			6.16 ± 1.10 [117]

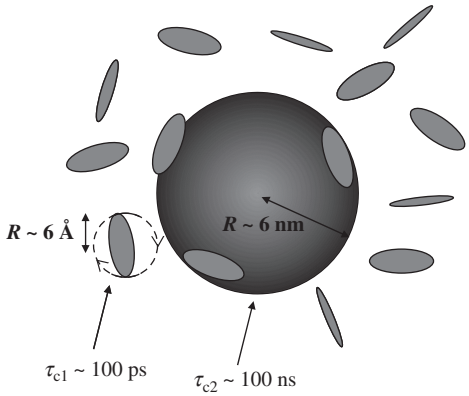

FIGURE 1.16 Depiction of the coexistence of dual anisotropy kinetics for the case of a fluorophore bound to a much larger nanoparticle and also unbound, both entities rotating freely under Brownian motion in solution. Since from Eq. (1.40) $\tau_c \propto R^3$, three orders of magnitude difference in rotational correlation time is observed for only one order of magnitude difference in radius. This helps reduce error propagation when measuring the radius. For the same reason, the dimensions of the fluorophore usually have negligible effect.

1.6.3 Application Example—Nanoparticle Metrology

Fluorescence anisotropy using fluorescence probes has undoubtedly been most widely used in biomolecular research for the study of structure and dynamics in protein [107] and membranes [118]. Here, we choose a different and in principle simpler example that concerns the measurement of nanoparticle size, and which uses the theory of multiple anisotropy decay components already described.

There has been a recent upsurge in interest in nanoparticles, concerning research not only into their new forms such as semiconductors and gold, but also into their older forms such as carbon and silica. Part of the interest lies in concern over the toxicology and environmental aspects of all types of nanoparticles, particularly those in the 1–10 nm range, which can easily traverse cellular membranes. Measuring such small sizes in in situ presents a significant challenge to metrology, though one in which fluorescence anisotropy decay is ideally suited.

The situation depicted by Figure 1.16 of a fluorophore bound to a much larger nanoparticle, and also unbound, can be realized using either electrostatic or covalent binding. Figure 1.17 illustrates a real example [119]. In Figure 1.17a, the nonbinding of anionic fluorescein to the anionic nanoparticles (rotational correlation time ∼200 ns) of LUDOX [55] silica AM30 is reflected with little change in the anisotropy decay when the dye is added to the colloid. Figure 1.17b shows how the cationic rhodamine 6G binds to the nanoparticles, but has too fast a fluorescence lifetime (∼ 4 ns) to effectively track the much slower depolarization as the nanoparticles rotate and is therefore still unsuitable for metrology purposes. Figure 1.17c shows that the binding and longer fluorescence lifetime (∼25 ns) of the cationic 6-methoxyquinolinium

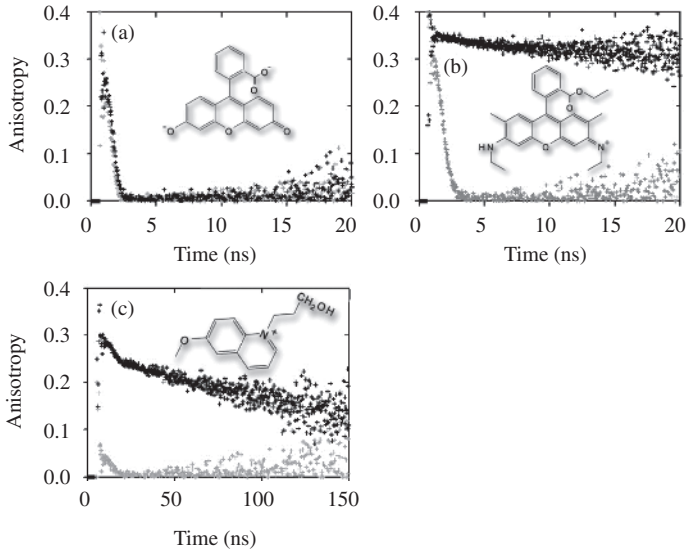

FIGURE 1.17 Effect on the fluorescence anisotropy decay (black data points) of adding different fluorophores to LUDOX [55] AM30 at pH 8.9: (a) Fluorescein, (b) rhodamine 6G, (c) 6-methoxyquinolinium (structures also shown). For comparison, the gray data points describe the dye rotation in methanol without LUDOX [119].

fluorophore are good enough to track the rotation, revealing the particle rotation and enabling the measurement of its radius.

The simplest case is when all the dye binds to the nanoparticle and then Eqs. (1.39) and (1.40) can be used. However, in this case, the microviscosity has to be already known or found from a separate anisotropy measurement or other means. If the anisotropy can be described by the presence of fluorophores that are both free and also bound to a nanoparticle, then a single anisotropy decay, analyzed using Eqs. (1.40) and (1.41), enables both the microviscosity of the medium and the nanoparticle radius to be conveniently determined in a single measurement [110,116]. However, things are not always so straight forward. Other effects, which may be present, and can influence the measured $r(t)$, include nanaoparticles aggregating and fluorophores wobbling on the nanoparticle, diffusing on the surface of the nanoparticle, aggregating on or off the nanoparticle, undergoing homo-FRET, and having a different fluorescence lifetime on and off the nanoparticle [119, 120]. Fortunately, some of these, though not all of these together, can usually be handled in the data analysis and, moreover, the sample can be designed at the outset to minimize such effects. Note also that having a complex multiexponential fluorescence decay tracking a nanoparticle rotation is not in itself any handicap whatsoever as long it is taken into account in the data analysis in Eq. (1.45).

One important difference between measuring anisotropy decay and fluorescence decay is the higher statistical precision (number of counts) needed in $I_{VV}(t)$ and

TABLE 1.4 Rotational parameters for LUDOX silica colloids labeled with a 6-methoxyquinolinium dye [120] and obtained by fitting the anisotropy decay to Eq. (1.44)

LUDOX	τ_{c1} (ns)	τ_{c2} (ns)	gr_0	r_0	χ^2	Peak in d_t	R_m (nm)	R_{fa} (nm)
SM30	24	65 ± 15	0.12	0.24	1.26	1×10^5	3.5	4.0 ± 0.4
AM30	17	273 ± 60	0.06	0.28	1.23	5×10^5	6.0	6.4 ± 0.5
AS40	10	1400 ± 590	0.07	0.28	1.27	1×10^6	12	11.0 ± 1.6

d_t is the peak count in the difference curve in Eq. (1.45). The data channel width was 28 ps. R_m is the manufacturers quoted value for the nanoparticle radius, most probably obtained using electron microscopy on the dry colloid. R_{fa} is the radius obtained from the τ_{c2} component of the fluorescence anisotropy decay. gr_0 is attributed to colloidal nanoparticle aggregates. τ_{c1} is too long to be free dye rotation, and may reflect dye wobbling and/or diffusing on the surface of the nanoparticle.

$I_{VH}(t)$ before a meaningful comparison of rotational models can be made. This is because it is not the absolute value, but the difference of $I_{VV}(t)$ and $I_{VH}(t)$ that is used in the anisotropy function (Eq. 1.36). The anisotropy measurements shown in Figure 1.17 were obtained using TCSPC with ∼10,000 counts in the peak channel of the difference curve [119] and this is adequate for many purposes. However, if a more complex model, such as that of Eq. (1.44) is to be deployed then much higher statistical precision is required. This is illustrated in Table 1.4 for a range of LUDOX colloids [120].

The nanoparticle radii obtained using fluorescence anisotropy decay and those from the manufacturer's data sheet [55] are in good agreement. It is also worth noting that in the case of AS40 $\tau_{c2}/\tau_f \sim 56$, which is way outside usual practice and only possible because of the large number of counts obtained in d_t.

This need for increasingly high statistical precision in the face of correlations between the fitted parameters, when more than one rotational correlation time is present, is the reason why the determination of rotational correlation time distributions (which would lead to useful nanoparticle size distributions in this example) is extremely difficult using fluorescence anisotropy decay. The problem is analogous to the difficulty of determining distance distributions in FRET in so far as unique solutions do not in general exist.

One way of improving the measurement capability is to increase the dynamic range of r_0 above its maximum of 0.4 by the use of multiphoton excitation, though this is at the expense of the simplicity of measurement as it requires femtosecond laser excitation [116]. Multiphoton excitation enforces a higher angular alignment of the absorption dipole with the plane of polarization of excitation with a probability $\cos^{2j}\alpha$ (Fig. 1.15), where j is the number of photons absorbed. For two- and three-photon excitation, r_0 increases from 0.4 for one-photon excitation to a maximum of 0.57 and 0.67, respectively, where β, the angle between the absorption and emission dipoles, is taken to be zero [116] as given by

$$r_{0n} = \frac{2j}{2j+3}\left[\frac{3}{2}\cos^2\beta - \frac{1}{2}\right]. \tag{1.47}$$

Given the paucity of standards for rotational time measurements, Table 1.4 suggests that well-defined silica colloids also have something to offer in this capacity. Equally there is a recognized lack of international standards for nanoparticle metrology in general. When compared with traditional methods for nanoparticle metrology such as small-angle neutron, X-ray, or light scattering and electron microscopy, fluorescence anisotropy decay offers an inexpensive alternative that enables measurements in situ, with sub-nanometer resolution, in the important 1–10 nm range.

Fluorescence anisotropy decay can be used to measure the size of other types of nanoparticles apart from silica, provided they can be labeled extrinsically with a fluorophore. Nanoparticle intrinsic fluorescence is not necessarily helpful because internal depolarization mechanisms, as in the case of carbon soot nanoparticles [121], can distort the measurement.

So far we have considered only the situation where the fluorescence lifetime associated with each rotational correlation time is the same. This is not always the case and such a change can lead to some peculiar anisotropy decay curves. For example, where a fluorescence lifetime associated with a longer rotational correlation time is longer than that of a faster fluorescence decay time associated with a faster rotational correlation time, that is, $\tau_{f1} < \tau_{f2}$ and $\tau_{c1} < \tau_{c2}$. In this case, $r(t)$ initially falls with time, goes through a dip, and then rises again as the longer lived fluorescence and rotational components start to dominate. Such effects have been observed and analyzed in protein and lipid bilayer membranes [122], often reflecting structural heterogeneity, but also with silica nanoparticles for free and bound dye [123]. This behavior can be successfully modeled by reworking Eqs. (1.37) and (1.38) to take account of the different fluorescence lifetime and then reformulating $r(t)$.

Finally, in addition to the examples already mentioned, both steady-state and time-resolved fluorescence anisotropy continue to find multifarious applications. These include metal ion sensing [124], drug compliance monitoring [125], beta-amyloid aggregation [126], surface modification [127], and pH meter measurement of nanoparticle growth during silica hydrogel production [128].

1.7 MICROSCOPY

Fluorescence microscopy is a noninvasive, nondestructive technique, capable of imaging at levels from a single molecule, cell, tissue, to human. No other method can interrogate molecules in living cells with anything remotely approaching fluorescence microscopy's combination of spatial resolution, sensitivity, selectivity, and dynamical insight. The capability to visualize biomolecules, by virtue of either intrinsic or extrinsic fluorescence, enables the study of elementary biochemical reactions in cells and, not surprisingly, this has become a prominent technique in biological research. Moreover, it is fair to say that fluorescence microscopy has enjoyed somewhat of a renaissance in recent years with a growth paralleled across fluorescence only by lifetime measurements. Much of this growth has been fueled by the translation of spectroscopy, molecular photophysics, and laser photonics as we will illustrate here.

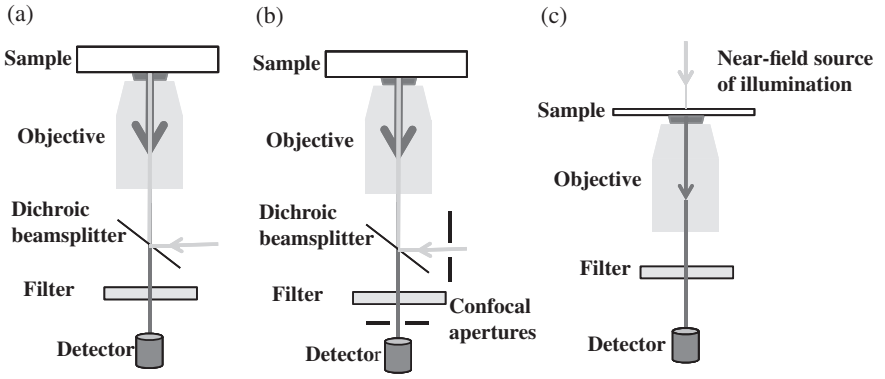

FIGURE 1.18 Schematics of some common fluorescence microscope configurations: (a) wide-field; (b) confocal; and (c) near-field.

1.7.1 Systems and Techniques

Figure 1.18 illustrates a schematic of some common fluorescence microscope configurations. Figure1.18a is representative of the most common configuration, a conventional epifluorescence (wide-field) microscope, which is traditionally operated with only incoherent optical excitation, such as from a high pressure mercury lamp fitted with a wavelength filter. The subsequent development of the confocal microscope and laser-based techniques greatly improved the spatial resolution and imaging capability of fluorescence microscopes. In a confocal microscope, as shown in Figure 1.18b, optical sections are illuminated through a pinhole aperture, and the fluorescence signal is channeled via another pinhole near the detector. The image is then compiled from laser scans of the surface. By means of the pinholes, the confocal microscope is able to discriminate against out-of-focus fluorescence and display-enhanced contrast in comparison with wide-field optical microscopes, allowing the reconstruction of three-dimensional (3D) structures from the images obtained. The development of 3D microscopy gained extra impetus with the introduction of Ti:sapphire ultrafast laser technology. This made multiphoton excitation much more routine than hitherto had been the case [129].

Multiphoton excitation microscopy generally uses long wavelength (near-IR) light and excites fluorescent dyes through an additive process, whereby the energy of two photons give the equivalent energy of one photon (cf. Fig. 1.1). While the advantages of multiphoton excitation in spectroscopy, for example, in increasing the dynamic range of anisotropy decay measurements, have already been mentioned (Eq. 1.47), further advantages accrue in microscopy. Using near-IR, multiphoton excitation minimizes the scattering in the sample, the background fluorescence, and photo-bleaching by virtue of the greater confinement of the excitation volume. The latter also facilitates the 3D imaging of sections over a greater optical penetration depth than is possible with one-photon confocal excitation [130].

The equivalent expression to one-photon absorption (Eq. 1.3) for j photons absorbed is nonlinear:

$$I_f = \eta(\Phi_f/j)Nd\sigma_j\rho^j, \tag{1.48}$$

where I_f is the rate of fluorescence, η the fluorescence detection efficiency, Φ_f/j the fluorescence quantum yield corrected for j-photon absorption, N the absorber number density (cm^{-3}), d the optical path length (cm), σ_j the absorption cross-section for j photons (cm^{2j} s^{j-1}) and ρ the excitation photon flux density (photons cm^{-2} s^{-1}, typically GW cm^{-2} over a 10-μm spot size).

From Eq. (1.48) it can be seen that the slope of $\log_e I_f$ versus $\log_e \rho$ should give a straight line of slope j. This is a useful method of determining the number of photon absorbed (see Section 1.7.2). Multiphoton excitation can also be used to selectively excite fluorophores and quantum states according to their different selection rules. Several reviews are available on the application of multiphoton excitation to biological molecules in microscopy [131] and in spectroscopy [132].

If fluorescence spectroscopy has progressed through the development of temporal resolution, then much of the push in fluorescence microscopy in recent years has been dominated by improving spatial resolution. This has been both in terms of sectioning in depth and lateral resolution such that sample volumes ∼10 fL can now be excited and this is sufficiently small for single molecules to be studied in isolation.

Conventional optical microscopes operate in the far field and have a diffraction-limited resolving power described by the Abbe criterion:

$$\Delta = \frac{\lambda}{2\mathrm{NA}}, \tag{1.49}$$

where Δ is the smallest possible resolvable distance between two point sources, given an emission wavelength, λ, and an imaging system with a numerical aperture (NA). NA is defined as $n\sin\theta$, where n is the refractive index of the imaging medium and θ is the half-angle of the maximum cone of light collected by the objective. This diffraction limit constrains the spatial resolution for visible wavelength to approximately 200–300 nm.

Progress in terms of depth resolution using multiphoton confocal microscopy has been complemented by other approaches. For example, total internal reflection fluorescence (TIRF) microscopy employs an evanescent wave generated when incident light is totally internally reflected at a glass–water/air interface to achieve selective illumination. Penetration depths of ≤100 nm in the low-refractive index medium have been achieved [133].

Improvements in lateral resolution have been obtained using a variety of techniques in recent years. This has created the exciting new area of single-molecule microscopy, which overcomes the ensemble smearing of information. This promises to provide heterogeneity and other fundamental information that might answer some of the big questions that underpin disease and therapeutics. For example, in protein does all protein of a given type fold by the same path? Can we monitor, and thereby

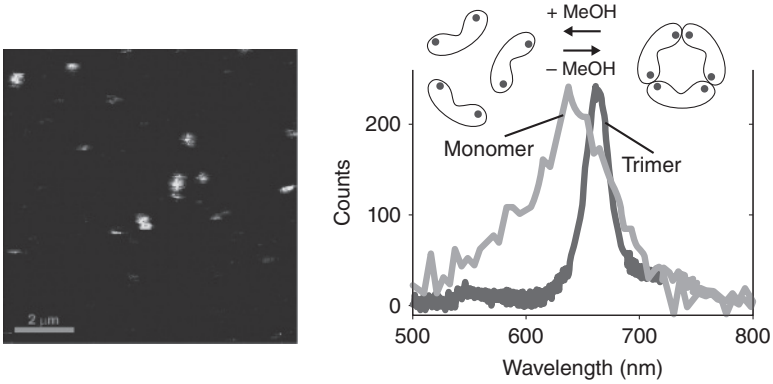

FIGURE 1.19 (a) Scanning confocal microscope images of single allophycocyanin (APC) molecules entrapped in hydrated pores of a thin silica film fabricated around the protein using the sol-gel process. The excitation wavelength is 532 nm. (b) The fluorescence spectra for the trimer (red) and monomer (blue) single molecule forms are shown. Dissociation of the trimer is induced by alcohol. Each APC unit contains two phycocyanobilin fluorophores, which are indicated by red dots. Reproduced from Reference 134 with permission from Springer Science + Business Media. (*For a color version of this figure, see the color plate section.*)

better understand, metabolism, disease, and therapeutics in cells at the level of binary molecular interactions? Figure 1.19 shows confocal microscope images and fluorescence spectra of a single protein aggregate and disaggregated monomer encapsulated for ease of observation in a hydrated silica nanopore [134].

Single-molecule microscopes come in different forms. Whatever their form, one of the underlying objectives is to enhance the fluorescence signal-to-noise ratio by reducing the lateral resolution and this can be adequately achieved using a confocal microscope. Such an arrangement is commonly used in fluorescence correlation spectroscopy (FCS), whereby a fluorescent entity (dye, protein, nanoparticle, etc.) is observed by a photon detector as it diffuses in solution in and out of the focal spot [135]. The autocorrelation function of the resultant fluorescence signal can be interpreted in terms of simple diffusion dynamics to provide information on size, aggregation, microviscosity, and diffusion constants that complement fluorescence quenching and anisotropy data. Two-photon excitation can also be used for excitation with confocal FCS in order to further confine the excitation volume [136].

Near-field scanning optical microscopy (NSOM) also enables single-molecule studies and breaks through the far-field resolution limit (Eq. 1.49), like TIRF, by exploiting the properties of evanescent waves (Fig. 1.18c). Here excitation is via a scanning single-mode optical fiber, which has a tapered tip with an internally reflective (aluminum-coated) sub-wavelength aperture that is held ∼10 nm from the sample. The resolution depends on the aperture diameter rather than the wavelength of the light in this case and can reach ∼50 nm [137], though the technique does not lend itself to depth profiling. Fluorescence lifetime measurements have been achieved

using NSOM [138], but early promise was not realized due to a lack of reproducibility in lifetime measurements caused by the plasmonic effect of the aluminized tip.

The ability to probe metabolism, disease, and therapeutics inside cells is a challenging task, but one in which single-molecule fluorescence, combined with spectroscopic techniques, has considerable potential to advance our knowledge. Several excellent reviews of fluorescence techniques applied to the study of single molecule are available [139–141].

One difficulty encountered in single-molecule microscopy is bleaching of the fluorophore during a measurement, since multiple excitations (often using MHz lasers) mean the likelihood of even low-probability nonemissive transitions being populated is high. For example, a single fluorophore with Φ_f as high as 0.9 might be seen to have a negligible probability for photobleaching p (say $\sim 10^{-6}$), but it only has to be excited $1/p$ times to be likely to bleach. Blinking also occurs where a fluorophore goes from the singlet excited state into a long lived triplet ("dark") state, which may or may not then repopulate the singlet state and allow the continuation of fluorescence. Figure 1.20 illustrates both these phenomena.

As already mentioned, oxygen is a ubiquitous quencher of fluorescence, and it also facilitates the bleaching of dye molecules. Although purging with nitrogen or freeze-pump-thaw cycles might be adequate for enhancing the fluorescence yield and lifetime in ensemble spectroscopy, oxygen scavenging chemicals are frequently used

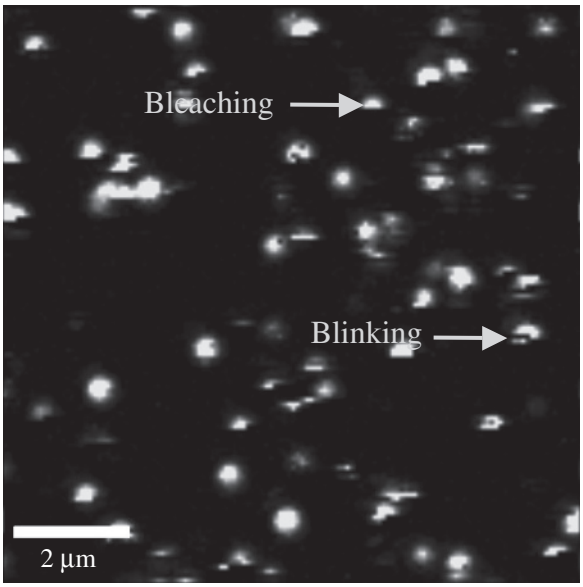

FIGURE 1.20 Laser scanning confocal microscope image of single rhodamine B molecules on a glass slide, illustrating the bleaching and blinking of dye molecules, these being a characteristic behavior of single molecules. The image acquisition time was 5.5 min using 40 nm × 40 nm pixels with an integration time of 5 ms. Reproduced from Reference 142.

in single-molecule microscopy in order to mitigate bleaching. Triplet quenchers can also be used to minimize blinking [143].

Perhaps somewhat ironically the quenching of fluorescence has been developed as means to enhance resolution in fluorescence microscopy. In the last two decades a whole new range of super-resolution light microscopy (nanoscopy) techniques have emerged for imaging in the far field and yet which break through the diffraction limit by means of active control of the fluorescence [144]. Stimulated emission depletion microscopy (STED) [145] was an early example overcoming the Abbe limitation (Eq. 1.49). Here the emission of fluorescence excited by an ultrafast laser pulse is confined to a region that is much smaller than that covered by the diffraction limit by following up the initial excitation with a further ultrafast excitation pulse that defines the resolution by depleting the fluorescence of dye within a doughnut around the central spot. Various other methods have been developed that are also based on the fundamental principle of active control of fluorescence, but using different mechanisms to achieve <20 nm resolution (i.e., superior to NSOM). These include photoactivated localization microscopy (PALM) [146], stochastic optical reconstruction microscopy (STORM) [147], and fluorescence PALM (FPALM) [148]. All these require a low concentration of well-separated fluorophores and then controlling their emission in order to avoid spatial overlap of emission that would otherwise blur the reconstruction of the image. Three-dimensional imaging is also possible and recently multicolor 3D super-resolution imaging has been demonstrated with a precision <10 nm by means of stochastically switching fluorophores [149]. Structured illumination microscopy [150] is an alternative approach and gives rapid 3D super-resolution imaging of cells by analyzing Moiré interference fringes.

Some quite spectacular and well-resolved images have been produced using these techniques and they are opening-up new possibilities for intracellular research in particular. Figure 1.21 illustrates this for images [151] obtained using direct photoactivation dSTORM [152], which uses direct excitation of a single fluorophore rather than a coupled pair of fluorophores. The super-resolution image typically generated is a computational reconstruction of the localized fluorophore density compiled from detecting fluorophores blinking.

The advantages of bringing more of the multidimensional nature of fluorescence to bear on microscopy became evident from quite early on. Traditionally, contrast in fluorescence microscopy is provided by fluorescence intensity. This is dependent on fluorophore extinction coefficient, quantum yield, the number of fluorophores present, and excitation intensity. The early fluorescence lifetime measurements with microscopes were only point-by-point single measurements [153] and the use of fluorescence lifetime as a means of contrast came later through the introduction of fluorescence lifetime imaging microscopy (FLIM). The advantages of fluorescence lifetimes mentioned in Section 1.4 also translate to microscopy. For example, the lifetime does not change with intensity; therefore, lifetime measurements are not dependent on the local concentration of fluorophore, bleaching, optical path of the microscope, excitation light intensity, or detection efficiency. Furthermore, the fluorescence lifetime usually depends on the intrinsic characteristics of the fluorophore and the local environment (e.g., microviscosity, pH, refractive index), as well as

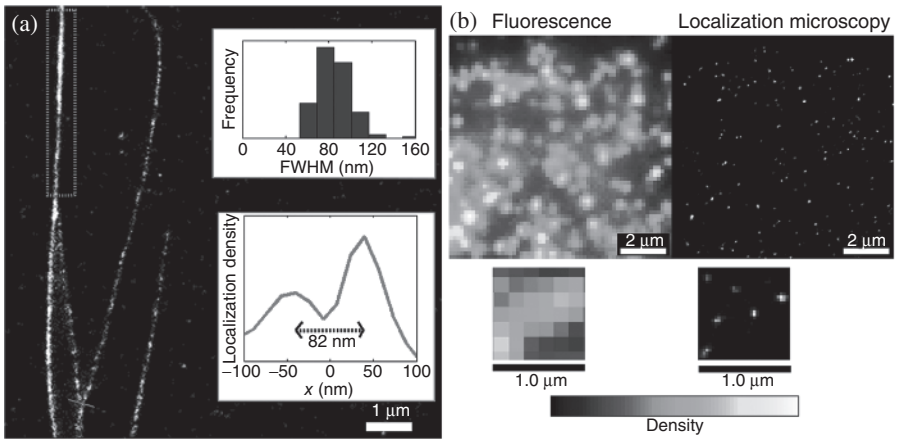

FIGURE 1.21 Super-resolution dSTORM images of (a) actin filaments stained with phalloidin-Alexa Fluor 647 on glass [151]. The spread in full width half maximum (FWHM) of the actin filament is shown in the upper boxed area. The localization density of a cross-section through two crossing filaments is shown in the lower boxed area. (b) Epidermal growth factor (EGF) is conjugated to Alexa Fluor 647 on HeLa cell surfaces, and bound to EGF receptors. Activation of EGF receptors results in dimerization of receptors and clustering into pits and vesicles with diameters ranging from 50 to 150 nm. Note how the localized microscopy image obtained by using a Gaussian intensity distribution at each point to find the center improves the resolution dramatically over the diffraction-limited fluorescence image that is actually recorded. Compare also with the improvement over the single-molecule confocal image without localization shown in Figure 1.20 on the same scale.

interactions with other molecules, such as through collisional or FRET quenching. Thus, as well as helping to distinguish spectrally overlapping fluorophores, imaging of the fluorescence lifetime can be used to probe the surroundings and dynamical processes of a fluorophore. FLIM can be integrated with wide-field, confocal, two-photon, and other microscopy systems and has been extensively reviewed [154, 155,156]. All the optical sources used for fluorescence lifetime spectroscopy can be used in FLIM. Similarly, for scanning FLIM systems, the same detectors as for spectroscopy can be used. Single-photon avalanche diodes (SPADs) are more widely used for detecting fluorescence in microscopy than in spectroscopy. SPADs have high detection efficiency and their small active area is more compatible with microscope than monochromator images and can also serve as a confocal aperture [157].

Both TCSPC and phase-modulation methods, as described in Section 1.4, can be used for FLIM. The relative merits of each in spectroscopy also translate to a large extent to microscopy, for example, speed of FLIM with wide-field phase-modulation and precision of TCSPC with confocal scanning. FRET [158] and anisotropy [159] (Sections 1.5 and 1.6, respectively) can be combined with FLIM, both as a further means of contrast and also for the molecular information they can provide, for example, intracellular microviscosity and refractive index using the Strickler-Berg expression (Eq. 1.12).

1.7.2 Application Example—Gold Nanorods in Cells

Nanoparticles have emerged in recent years as providing new approaches to imaging, sensing, drug delivery, and therapeutics [160]. Noble metals and quantum dots in particular have been shown to complement aromatic fluorophores, not only by generating their own distinctive emission but also by modifying aromatic fluorescence [161]. Just as Raman has benefitted from surface plasmon resonance (SPR) enhancement, so too can fluorescence be enhanced and plasmonics tuned to further good effect [162, 163].

In its bulk form, gold has an extremely low luminescence quantum yield ($\sim 10^{-10}$) but in nanoparticle form it not only has a workable quantum yield, but has advantages over conventional aromatic probes in so far as it is less cytotoxic and does not photobleach. In the context of fluorescence the interest in nanoparticles, already mentioned in Section 1.6.3, is primarily twofold. First, as more needs to be learned about the intra- and intercellular transport properties of nanoparticles with respect to toxicity [164], gold provides a useful paradigm. Second, the intracellular imaging properties of gold nanoparticles offer a new approach to this fundamental area of biology.

As compared to in the bulk, gold spheres of dimensions <5 nm have been found to have a much enhanced quantum yield of $\sim 10^{-5}$–10^{-4}, which is thought to be due to electron-hole recombination following absorption of a photon to promote an electron from the narrow d band to the sp band above the Fermi level [165]. Gold nanorods were subsequently found to have an even higher quantum yield of ($\sim 10^{-4}$ to 10^{-3}) when exciting the transverse surface plasmon mode [166]. One-photon excitation is convenient, but a higher quantum yield would be desirable for cellular imaging purposes. Multiphoton excitation of surface plasmon modes to obtain resonant coupling in gold nanorods has also been demonstrated and shown to offer comparable emission intensity to aromatic flurophores [167, 168]. This significant development brought the additional advantages of multiphoton excitation to bear on cellular microscopy studies with gold, as we illustrate below. More recently, quantum-confined fluorescent gold clusters (a few tens of atoms with a radius $\leq$1 nm) have been found to have "molecular-like" properties and relatively intense emission upon one-photon excitation. The clusters are synthesized and stabilized in protein and were recently reviewed [169].

The seeded growth method is typically used for synthesizing gold nanorods [170]. Typically, the steps are 2.5 mL $HAuCl_4 \times 3H_2O$ (0.001 M) and 0.6 mL ice-cold $NaBH_4$ (0.01 M) are added into 7.5 mL cetyltrimethylammonium bromide (CTAB) (0.1 M) to prepare the seed solution. The growth solution is then synthesized by adding 0.15 M BDAC, 50 mL $HAuCl_4 \times 3H_2O$ (0.001 M), 2 mL $AgNO_3$ (0.004 M), and 700 μL ascorbic acid (0.778 M) to 50 mL CTAB solution (0.1 M). The 80 μl seed solution is then injected into the growth solution to grow gold nanorods.

The absorption spectrum of gold nanorods is characterized by two SPR absorption bands that depend on the aspect ratio. Figure 1.22 shows a scanning electron microscope (SEM) image of gold nanorods, the emission power dependence confirming the two-photon nature of the fs Ti:sapphire laser excitation (Eq. 1.48) and typical absorption spectra featuring longitudinal and weaker transverse plasmon modes over a range of aspect ratios.

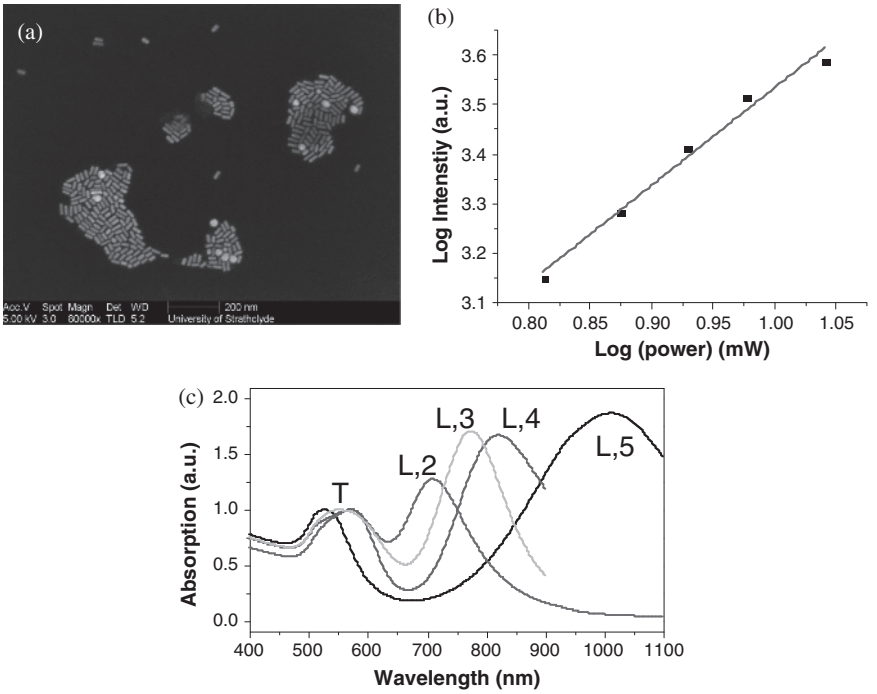

FIGURE 1.22 Gold nanorods: (a) SEM measurement. (b) Emission intensity dependence on laser excitation power giving a slope of 1.97, confirming two-photon excitation at 750 nm. (c) Plasmon absorption bands showing transverse (T) and longitudinal (L, AR) modes for aspect ratios (AR) of 2, 3, 4, and 5. (*For a color version of this figure, see the color plate section.*)

Gold nanorods are of great interest for biological imaging due to their remarkable absorption and emission in the visible and near-IR regions when enhanced by SPR. Especially, the absorption band between 700 and 900 nm corresponding to the longitudinal SPR when excited by two photons in order to generate luminescence of high intensity that is compatible with the spectral window in cells and tissue. Two-photon emission from gold nanorods has been found to be sensitive to the polarization of the incident excitation and has enabled single particle imaging. All these properties make gold nanorods attractive probes for in vitro and in vivo imaging and their properties, applications, and synthesis have been reviewed [171, 172].

To prepare cell culture samples, gold nanorods dispersions are centrifuged and redispersed in deionized water. In our example here Madin-Darby canine kidney (MDCK) cells are then treated with 100 μL of gold nanorod solution and incubated for 3 h under standard cell culture conditions at 37°C and 5% CO_2. The cells are washed and can then be stained with a fluorophore, in our case 4′,6-diamidino-2-phenylindole (DAPI). The sample is then dispersed on a glass slide with a cover slip for imaging.

Figure 1.23 compares the intensity image and lifetime image of gold nanorods in MDCK cells. The elliptical shapes in (a) and (b) correspond to nuclei stained

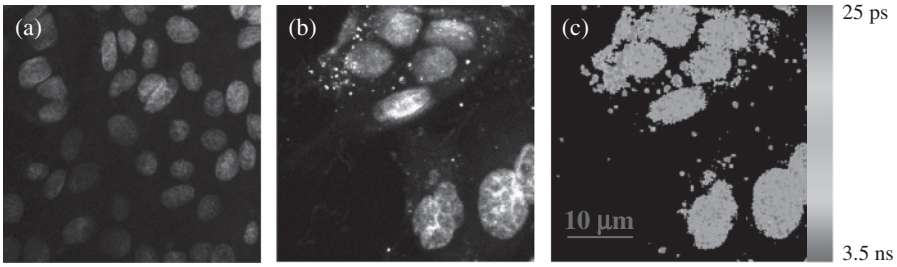

FIGURE 1.23 Two-photon excited MDCK cells stained with DAPI: Fluorescence intensity image (a) without gold nanorods and (b) with gold nanorods. (c) FLIM image. Images are obtained using two-photon 750 nm excitation in the longitudinal plasmon band with emission collected over 535–590 nm. The scanning areas are (a) 133 μm × 133 μm, for (b) and (c) 67 μm × 67 μm 173. (*For a color version of this figure, see the color plate section.*)

by DAPI, and the bright spots in (b) are due to two-photon excited emission from gold nanorods which are not present in (a). The fluorescence lifetime of DAPI in cells is found to be typically a few nanoseconds, while the two-photon excited decay time of gold nanorods is measured here to be <100 ps (limited by the instrumental resolution), as confirmed by a FLIM study of pure gold nanorods on a glass slide and time-resolved luminescence measurement of gold nanorods in a cuvette. The FLIM image, (c), taken from the same sample area as in (b), with different coded colors representing different lifetimes, clearly distinguishes the emissions from DAPI (blue) and gold nanorods (orange). Previous work has shown that in fact the decay constant associated with the gold nanorod emission is as low as a few ps [174, 175]. Figure 1.23 illustrates how fluorescence lifetime can provide a highly selective contrast parameter for gold nanorods with respect to dye stains and endogenous fluorophores.

Opportunities with energy transfer to fluorophores are also available with gold nanorods. This is illustrated in Figure 1.24a, again using a two-photon FLIM image of gold nanorods incubated in MDCK cells [176]. Concentrating on the detailed structures, lifetime decays from rectangular regions labeled A and B are displayed in Figure 1.24b. A decay curve of only DAPI in the cell culture is plotted as a reference, and is described well by a single-exponential decay with a lifetime of 2.5 ns. Both decay curves in the regions A and B can be described by a biexponential model, with a shorter component less than 100 ps ascribed to gold nanorods and a longer ns component to DAPI. For decay curve in region A, the longer component is 2.5 ns. A reduced lifetime component of 0.9 ns for DAPI is found for the decay curve derived from region B, indicating energy transfer between DAPI and gold nanorods in this region.

Clearly, as well as using the ultrafast decay time of gold nanorods for contrast, some of the other properties of gold nanorods such as dual plasmon modes, polarization dependence of excitation, FRET and ability to conjugate can all be brought to bear on intracellular studies. Finally, although previously mentioned here only briefly, gold

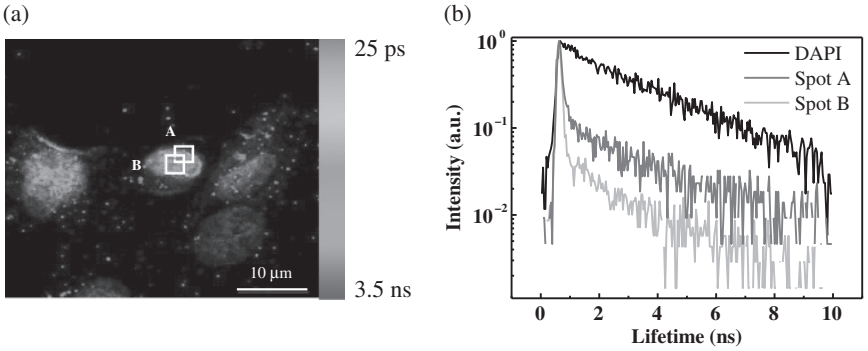

FIGURE 1.24 (a) Two-photon excited FLIM image of GNRs incubated in MDCK cells. Experimental conditions are as for Figure 1.23, but with a scanning area of 67 μm × 67 μm. (b) Normalized fluorescence decay curves derived from regions A and B, with the fluorescence decay curve of DAPI shown for reference. Reproduced from Reference 176 with permission from AIP Publishing LLC. (*For a color version of this figure, see the color plate section.*)

nanoclusters of a few atoms synthesized in protein [169] would also seem to have much to offer, for example in intracellular sensing of metal ions [177].

1.8 CONCLUSIONS

In this chapter, we have surveyed some of the main capabilities, techniques, and measurements that are enabled by fluorescence. This has been supported by references to both original articles and reviews of each topic. Space constraints dictate that we are unable to provide the rigor of complete and dedicated texts [1–4], but we hope that we have been able to go some way toward bridging the gap between the fundamental principles and the perspectives and opportunities generated by modern day applications of fluorescence [178].

Although there are important theoretical aspects still to be solved, the field of fluorescence is largely driven by its experimental applications. One important experimental aspect, that has so far received comparatively scant attention, is the methodology and tricks-of-the-trade that are so essential for good practice in fluorescence measurements. A recent text seeks to address such a requirement, including all the main areas covered here, and provides a useful complement to the present body of literature [179].

ACKNOWLEDGMENTS

The authors wish to acknowledge the research support of EPSRC, BBSRC, and SFC. They are also grateful to Dr. Ashok Ganesan for granting permission to include Figure 1.3.

REFERENCES

[1] I. B. Berlman, *Handbook of Fluorescence Spectra of Aromatic Molecules*, 2nd ed. (Academic Press, New York, 1971).

[2] J. B. Birks, *Photophysics of Aromatic Molecules* (Wiley-Interscience, London, 1970).

[3] J. R. Lakowicz, *Principles of Fluorescence Spectroscopy*, 3rd ed. (Springer, New York, 2006).

[4] B. Valeur, *Molecular Fluorescence Principles and Applications*, 2nd ed. (Wiley-VCH, Weinheim, 2012).

[5] C. A. Parker and W. T. Rees, "Correction of fluorescence spectra and measurement of fluorescence quantum efficiency," *Analyst* **85**, 587–600 (1960).

[6] W. H. Melhuish, "Calibration of spectrofluorimeters for measuring corrected emission spectra," *J. Opt. Sci. Am.* **52**(11), 1256–1258 (1962).

[7] T. B. Fitzpatrick, G. Szabo, M. M. Wick, and J. A. Parrish, "Biochemistry and physiology of melanin pigmentation," in *Biochemistry and Physiology of the Skin*, edited by L. A. Goldsmith (Oxford University Press, New York, 1983), pp. 687–712.

[8] P. Meredith and T. Sarna, "The physical and chemical properties of eumelanin,"*Pigm. Cell Res.* **19**, 572–594 (2006).

[9] W. R. Ware and W. Rothman, "Relative fluorescence quantum yields using an integrating sphere. The quantum yield of 9,10-diphenylanthracene in cyclohexane," *Chem. Phys. Lett.* **39**(3), 449–453 (1976).

[10] C. Würth, M. Grabolle, J. Pauli, M. Spieles, and U. Resch-Genger, "Relative and absolute determination of fluorescence quantum yields of transparent samples," *Nat. Prot.* **8**, 1535–1550 (2013).

[11] W. H. Melhuish, "Distribution of fluorescence from a disk-shaped cuvette," *J. Opt. Sci. Am.* **51**, 278–279 (1961).

[12] D. J. S. Birch and R. E. Imhof, "Fluorescence lifetimes and relative quantum yields of 9,10-diphenylanthracene in dilute solutions of cyclohexane and benzene," *Chem. Phys. Lett.* **32**, 56–58 (1975).

[13] I. W. Hamley, "Peptide fibrillization," *Angew. Chemie. Int. Ed.* **46**, 8128–8147 (2007).

[14] A. K. Geim, and K. S. Novoselov, "The rise of graphene," *Nat. Mater.* **6**, 183–191 (2007).

[15] H. LeVine III, "Thioflavine T interaction with synthetic Alzheimer's disease β-amyloid peptides: detection of amyloid aggregation in solution," *Protein Sci.* **2**, 404–410 (1993).

[16] V. I. Stsiapura, A. A. Maskevich, V. A. Kuzmitsky, V. N. Uversky, I. M. Kuznetsova, and K. K. Turoverov, "Thioflavin T as a molecular rotor: fluorescent properties of thioflavin T in solvents with different viscosity," *J. Phys. Chem. B* **112**(49), 15893–15902 (2008).

[17] O. J. Rolinski, M. Amaro, and D. J. S. Birch, "Early detection of amyloid aggregation using intrinsic fluorescence," *Biosens. Bioelectron.* **25**(10), 2249–2252 (2010).

[18] J. Mohanty, S. D. Choudhury, H. Pal, and A. C. Bhasikuttan, "Early detection of insulin fibrillation: a fluorescence lifetime assay to probe the pre-fibrillar regime," *Chem. Commun.* **48**, 2403–2405 (2012).

[19] A. A. R. Watt, J. P. Bothma, and P. Meredith, "The supramolecular structure of melanin," *Soft Matter.* **5**, 3754–3760 (2009).

[20] J. Sutter, T. Bidláková, J. Karolin, and D. J. S. Birch, "Eumelanin kinetics and sheet structure," *Appl. Phys. Lett.* **100**, 13701 (2012).

[21] N. Benseny-Cases, M. Cócera, and J. Cladera, "Conversion of non-fibrillar β-sheet oligomers into amyloid fibrils in Alzheimer's disease peptide aggregation," *Biochem. Biophys. Commun.* **361**, 916–921 (2007).

[22] S. J. Strickler and R. A. Berg, "Relationship between absorption intensity and fluorescence lifetime of molecules," *J. Chem. Phys.* **37**, 814–822 (1962).

[23] K. Suhling, J. Siegel, D. Phillips, P. M. W. French, S. Leveque-Fort, S. E. D. Webb, and D. M. Davis, "Imaging the environment of green fluorescent protein," *Biophys. J.* **83**(6), 3589–3595 (2002).

[24] W. R. Ware and B. A. Baldwin, "Absorption intensity and fluorescence lifetimes of molecules," *J. Chem. Phys.* **40**(6), 1703–1705 (1964).

[25] D. V. O'Connor, S. R. Meech, and D. Phillips, "Complex fluorescence decay of quinine bisulphate in aqueous sulphuric acid solution," *Chem. Phys. Lett.* **88**, 22–26 (1982).

[26] J. B. Birks, "Radiative lifetime anomalies," *Z. Phys. Chem.* **101**, 91–104 (1976).

[27] D. J. S. Birch and R. E. Imhof, "The origin of fluorescence from trans-trans diphenylbutadiene," *Chem. Phys. Lett.* **88**, 243–247 (1982).

[28] J. R. Lakowicz, G. Laczko, H. Cherek, E. Gratton, and M. Linkeman, "Analysis of fluorescence decay kinetics from variable-frequency phase shift and modulation data," *Biophys. J.* **46**, 463–477 (1984).

[29] D. W. Piston, G. Marriott, T. Radivoyevich, R. M. Clegg, T. M. Jovin, and E. Gratton, "Wide-band acousto-optic light modulator frequency domain fluorometry and phosphorimetry," *Rev. Sci. Instrum.* **60**(8), 2596–2600 (1989).

[30] D. V. O'Connor and D. Phillips. *Time-Correlated Single Photon Counting* (Academic Press, London, 1984).

[31] D. J. S. Birch and R. E. Imhof, "Time-domain fluorescence spectroscopy using time-correlated single-photon counting," in *Topics in Fluorescence Spectroscopy*, Vol. 1: Techniques, edited by J. R. Lakowicz (Plenum Press, New York, 1991), pp. 1–95.

[32] L. M. Bollinger and G. E. Thomas, "Measurement of the time-dependence of scintillation intensity by a delayed coincidence method," *Rev. Sci. Instrum.* **32**, 1044–1052 (1961).

[33] G. Hungerford and D. J. S. Birch, "Single-photon timing detectors for fluorescence lifetime spectroscopy," *Meas. Sci. Technol.* **7**, 121–135 (1996).

[34] M. D. Eisaman, J. Fan, A. Migdall, and S. V. Polyakov, "Single-photon sources and detectors," *Rev. Sci. Instrum.* **82**, 071101 (2011).

[35] D. J. S. Birch and R. E. Imhof, "Coaxial nanosecond flashlamp," *Rev. Sci. Instrum.* **52**, 1206–1212 (1981).

[36] D. J. S. Birch and R. E. Imhof, "A single-photon counting fluorescence decay-time spectrometer," *J. Phys. E. Sci. Instrum.* **10**, 1044–1049 (1977).

[37] T. Imasaka, A. Yoshitake, K. Hirata, Y. Kawabata, and N. Ishibashi, "Pulsed semiconductor laser fluorometry for lifetime measurements," *Anal. Chem.* **57**, 947–949 (1985).

[38] S. Nakamura, "InGaN-based violet laser diodes," *Semicon. Sci. Technol.* **14**, R27–R40 (1999).

[39] W. J. O'Hagan, M. McKenna, D. C. Sherrington, O. J. Rolinski, and D. J. S. Birch, "MHz LED source for nanosecond fluorescence sensing," *Meas. Sci. Technol.* **13**, 84–91 (2002).

[40] C. D. McGuinness, K. Sagoo, D. McLoskey, and D. J. S. Birch, "A new sub-nanosecond LED at 280 nm: application to protein fluorescence," *Meas. Sci. Technol.* **15**, L19–L22 (2004).

[41] C. D. McGuinness, K. Sagoo, D. McLoskey, and D. J. S. Birch, "Selective excitation of tryptophan fluorescence decay in proteins using a subnanosecond 295 nm light-emitting diode and time-correlated single-photon counting," *Appl. Phys. Lett.* **86**, 261911–261913 (2005).

[42] C. D. McGuinness, A. M. Macmillan, K. Sagoo, D. McLoskey, and D. J. S. Birch, "Excitation of fluorescence decay using a 265 nm pulsed light-emitting diode: evidence for aqueous phenylalanine rotamers," *Appl. Phys. Lett.* **89**, 063901–063903 (2006).

[43] D. McLoskey, D. Campbell, A. Allison, and G. Hungerford, "Fast-time-correlated single-photon counting fluorescence lifetime acquisition using a 100 MHz semiconductor excitation source," *Meas. Sci. Technol.* **22**, 067001 (2011).

[44] P. B. Coates, "The correction for photon "pile-up" in the measurement of radiative lifetimes," *J. Phys. E. Sci. Instrum.* **1**, 878–879 (1968).

[45] C. C. Davis and T. A. King, "Single photon counting pileup corrections for time-varying light sources," *Rev. Sci. Instrum.* **41**(3), 407–408 (1970).

[46] W. Becker, "*Advanced Time-Correlated Single Photon Counting Techniques* (Springer, Berlin, 2005).

[47] D. J. S. Birch, R. E. Imhof, and A. Dutch, "Pulse fluorometry using simultaneous acquisition of fluorescence and excitation," *Rev. Sci. Instrum.* **55**, 1255–1264 (1984).

[48] D. J. S. Birch, A. S. Holmes, J. R. Gilchrist, R. E. Imhof, S. M. Al-Alawi, and B. Nadolski, "A Multiplexed single photon instrument for routine measurement of time-resolved fluorescence anisotropy," *J. Phys. E. Sci. Instrum.* **20**, 471–473 (1987).

[49] D. J. S. Birch, A. S. Holmes, R. E. Imhof, B. Z. Nadolski, and K. Suhling, "Multiplexed array fluorometry," *J. Phys. E. Sci. Instrum.* **21**, 415–417 (1988).

[50] W. Becker, A. Bergmann, E. Haustein, Z. Petrasek, P. Schwille, C. Biskup, L. Kelbauskas, K. Benndorf, N. Klöcker, T. Anhut, et al., "Fluorescence lifetime images and correlation spectra obtained by multidimensional time-correlated single photon counting," *Micr. Res. Tech.* **69**, 186–195 (2006).

[51] W. Becker, A. Bergmann, and C. Biskup, "Multispectral fluorescence lifetime imaging by TCSPC," *Micr. Res. Tech.* **70**, 403–409 (2007).

[52] D. McLoskey, D. J. S. Birch, A. Sanderson, K. Suhling, E. Welch, and P. J. Hicks, "Multiplexed single-photon counting, I. A time-correlated fluorescence lifetime camera," *Rev. Sci. Instrum.* **67**, 2228–2237 (1996).

[53] B. R. Rae, C. Griffin, J. McKendry, J. M. Girkin, H. X. Zhang, E. Gu, D. Renshaw, E. Charlton, M. D. Dawson, and R. K. Henderson, "CMOS driven micro-pixel LEDs integrated with single photon avalanche diodes for time resolved fluorescence measurements," *J. Phys. D. Appl. Phys.* **41**, 094011 (2008).

[54] Y. Wang, B. R. Rae, R. K. Henderson, Z. Gong, J. McKendry, E. Gu, M. D. Dawson, G. A. Turnbull, and I. D. W. Samuel, "Ultra-portable explosives sensor based on a CMOS fluorescence lifetime analysis micro-system," *AIP Adv.* **1**, 032115 (2011).

[55] DuPont. *LUDOX Colloidal Silica: Properties, Uses, Storage and Handling: Data Sheets* (DuPont, 1987).

[56] P. R. Bevington. *Data Reduction and Error Analysis for the Physical Sciences* (McGraw-Hill, New York, 1969).

[57] A. K. Livesey and J. Skilling, "Maximum entropy method," *Acta Crystallogr.* **A41**, 113–122 (1985).

[58] C. Zander, M. Sauer, K. H. Drexhage, D.-S. Ko, A. Schulz, J. Wolfrum, L. Brand, C. Eggeling, and C. A. M. Seidel, "Detection and characterization of single molecules in aqueous solution," *Appl. Phys. B* **63**, 517–523 (1996).

[59] N. Boens, W. Qin, N. Basaric, J. Hofkens, M. Ameloot, J. Pouget, J.-P. Lefevre, B. Valeur, E. Gratton, M. VandeVen, et al., "Fluorescence lifetime standards for time and frequency domain fluorescence spectroscopy," *Anal. Chem.* **79**, 2137–2149 (2007).

[60] J. C. Pickup, "Diabetic control and its measurement," in *Textbook of Diabetes*, 3rd ed. edited by J. C. Pickup and G. Williams (Blackwell, Oxford, 2003), pp. 34.1–34.17.

[61] J. C. Pickup, F. Hussain, N. D. Evans, and N. Sachedina, "In vivo glucose monitoring: the clinical reality and the promise," *Biosens. Bioelectron.* **20**, 1897–1902 (2005).

[62] A. Ciudin, C. Hernandez, and R. Simo, "Non-invasive methods of glucose measurement: current status and future perspectives," *Curr. Diab. Rev.* **8**, 48–54 (2012).

[63] N. D. Evans, L. Gnudi, O. J. Rolinski, D. J. S. Birch, and J. C. Pickup, "Non-invasive glucose monitoring by NAD(P)H autofluorescence spectroscopy in fibroblasts and adipocytes: a model for skin glucose sensing," *Diabet. Technol. Ther.* **5**, 807–816 (2003).

[64] T. D. James, K. R. R. A. S. Sandanayake, and S. Shinkai, "A glucose-selective molecular fluorescence sensor," *Angew. Chem. Int. Ed.* **33**, 2207–2209 (1994).

[65] S. Mansouri and J. S. Schultz, "A miniature optical glucose sensor based on affinity binding," *Biotechnology* **2**, 885–890 (1984).

[66] P. W. Barons, R. S. Parker, and M. S. Strano, "In-vivo fluorescence detection of glucose using a single-walled carbon nanotube optical sensor: design, fluorophore properties, advantages, and disadvantages," *Anal. Chem.* **77**, 7556–7562 (2005).

[67] F. Hussain, D. J. S. Birch, and J. C. Pickup, "Glucose sensing based on the intrinsic fluorescence of sol-gel immobilized yeast hexokinase," *Anal. Biochem.* **339**, 137–143 (2005).

[68] T. Tolosa, I. Gryczynski, L. R. Eichhorn, J. D. Dattelbaum, F. N. Castellano, G. Rao, and J. R. Lakowicz, "Glucose sensor for low-cost lifetime-based sensing using a genetically engineered protein," *Anal. Biochem.* **267**, 114–120 (1999).

[69] O. J. Rolinski, D. J. S Birch, L. J. McCartney, and J. C. Pickup, "A time-resolved near-infra-red fluorescence assay for glucose: opportunities for trans-dermal sensing," *J. Photochem. Photobiol. B* **54**, 26–34 (2000).

[70] K. J. Thomas, D. B. Sherman, T. J. Amiss, S. A. Andaluz, and J. B. Pitner, "A long wavelength fluorescence glucose biosensor based on bioconjugates of galactose/glucose binding protein and Nile Red derivatives," *Diabet. Technol. Ther.* **8**, 261–268 (2006).

[71] F. Khan, L. Gnudi, and J. C. Pickup, "Fluorescence-based sensing of glucose using engineered glucose/galactose-binding protein: a comparison of fluorescence resonance energy transfer and environmentally sensitive dye labelling strategies," *Biochem. Biophys. Res. Commun.* **365**, 102–106 (2008).

[72] T. Saxl, F. Khan, M. Ferla, D. Birch, and J. Pickup. "A fluorescence lifetime-based fibre-optic glucose sensor using glucose/galactose-binding protein," *Analyst* **136**, 968–972 (2011).

[73] K. Weidemaier, A. Lastovich, S. Keith, J. B. Pitner, M. Sistare, R. Jacobson, and D. Kurisko, "Multi-day pre-clinical demonstration of glucose/galactose binding protein-based fiber optic sensor," *Biosens. Bioelectron.* **26**(10), 4117–4123 (2011).

[74] J. C. Pickup, Z.-L. Zhi, F. Khan, T. Saxl, and D. J. S. Birch, "Nanomedicine and its potential in diabetes research and practice. Diabetes/Metabolism," *Res. Rev.* **24**, 604–610 (2008).

[75] M. De Miguel, M. Alvaro, and H. Garcia, "Graphene as a quencher of electronic excited states of photochemical probes," *Langmuir* **28**, 2849–2857.

[76] D. K. Singh, P. K. Iyer, and P. K. Giri, "Role of molecular interactions and structural defects in the efficient fluorescence quenching by carbon nanotubes," *Carbon* **50**, 4495–4505 (2012).

[77] C. Preininger, I. Klimant, and O. S. Wolfbeis, "Optical fiber sensor for biological oxygen demand," *Anal. Chem.* **66**, 1841–1846 (1994).

[78] J. N. Demas and B. A. DeGraff, "Design and applications of highly luminescent transition metal complexes," in *Topics in Fluorescence Spectroscopy*, Vol. 4: Probe Design and Chemical Sensing, edited by J. R. Lakowicz (Plenum Press, New York, 1994), pp. 71–107.

[79] C. D. Geddes, K. Apperson, J. Karolin, and D. J. S. Birch, "Chloride sensitive fluorescent indicators," *Anal. Biochem.* **293**, 60–66 (2001).

[80] F. Kielar, C. P. Montgomery, E. J. New, D. Parker, R. A. Poole, S. L. Richardson, and P. A. Stenson, "A mechanistic study of the dynamic quenching of the excited state of europium(III) and terbium(III) microcyclic complexes by charge- or electron transfer," *Org. Biomol. Chem.* **5**, 2975–2982 (2007).

[81] O. S. Wolfbeis and W. Trettnak, "Fluorescence quenching of acridinium and 6-methoxyquinolinium ions by Pb^{2+}, Hg^{2+}, Cu^{2+}, Ag^{2+} and hydrogen sulphide," *Spectrochim. Acta A* **43**, 405–408 (1987).

[82] B. Juskowiak, "Efficient quenching of the fluorescence of binapthyl-based amphiphiles by mercury(II) complexes," *Anal. Chim. Acta* **320**, 115–124 (1996).

[83] S. P. Van and G. S. Hammond, "Amine quenching of aromatic fluorescence and fluorescent exciplexes," *J. Am. Chem. Soc.* **100**(12), 3895–3902 (1978).

[84] D. M. Davis, D. McLoskey, D. J. S. Birch, P. R. Gellert, R. S. Kittlety, and R. M. Swart, "The fluorescence and circular dichroism of proteins in reverse micelles: application to the photophysics of human serum albumin and *N*-acetyl-l-tryptophanamide," *Biophys. Chem.* **60**, 63–77 (1996).

[85] M. Smoluchowski, "Search for a mathematical theory of kinetic coagulation of colloid solutions," *Z. Phys. Chem.* **92**, 129–168 (1917).

[86] J. R. Lakowicz, M. L. Johnson, N. Joshi, I. Gryczynski, and G. Laczko, "Transient effects in quenching detected by harmonic-content frequency domain fluorometry," *Chem. Phys. Lett.* **131**, 343–348 (1986).

[87] D. J. S. Birch, A. Dutch, R. E. Imhof, B. Nadolski, and I. Soutar, "The effect of transient quenching on the excimer kinetics of 2,5-diphenyloxazole," *J. Photochem.* **38**, 239–254 (1987).

[88] N. Periasamy, S. Doraiswany, B. Venkataraman, and G. R. Fleming, "Diffusion controlled reactions: experimental verification of the time-dependent rate equation," *J. Chem. Phys.* **89**(8), 4799–4806 (1988).

[89] L. Stryer and R. P. Haugland, "Energy transfer: a spectroscopic ruler," *Proc. Natl. Acad. Sci. USA* **58**, 719–726 (1967).

[90] S. Saini, G. Srinivas, and B. Bagchi, "Distance and orientation dependence of excitation energy transfer: from molecular systems to metal nanoparticles," *J. Phys. Chem. B* **113**(7), 1817–1832 (2009).

[91] A. Iqbal, S. Arslan, B. Okumus, T. J. Wilson, G. Giraud, D. G. Norman, T. Ha, and D. M. J. Lilley, "Orientation dependence in fluorescent energy transfer between Cy3 and Cy5 terminally-attached to double-stranded nucleic acids," *Proc. Natl. Acad. Sci. USA* **105**, 11176–11181 (2008).

[92] J. Klafter and A. Blumen, "Direct energy transfer in restricted geometries," *J. Lumin.* **34**, 77–82 (1985).

[93] O. J. Rolinski and D. J. S. Birch, "Structural sensing using fluorescence nanotomography," *J. Chem. Phys.* **116**(23), 10411–10418 (2002).

[94] O. J. Rolinski, D. J. S. Birch, and A. S. Holmes, "Metal ion quenching kinetics of DTDCI in viscous solution and Nafion membranes: model system for near infrared fluorescence sensing," *J. Biomed. Opt.* **3**(3), 346–356 (1998).

[95] D. J. S. Birch, O. J. Rolinski, and D. Hatrick, "Fluorescence lifetime sensor of copper ions in water," *Rev. Sci. Instrum.* **67**(8), 2732–2737 (1996).

[96] U. Gösele, M. Hauser, U. K. A. Klein, and R. Frey, "Diffusion at long range energy transfer," *Chem. Phys. Lett.* **34**, 519–522 (1975).

[97] J. W. Taraska, M. C. Puljung, and W. N. Zagotta, "Short-distance probes for protein backbone structure based on energy transfer between bimane and transition metal ions," *Proc. Natl. Acad. Sci. USA* **106**(38), 16227–16232 (2009).

[98] J. W. Taraska, "Mapping membrane protein structure with fluorescence," *Curr. Opin. Struct. Biol.* **22**, 507–513 (2012).

[99] O. J. Rolinski and D. J. S. Birch, "A fluorescence lifetime sensor for Cu(I) ions," *Meas. Sci. Technol.* **10**, 127–136 (1999).

[100] R. B. Thompson and M. W. Patchan, "Lifetime-based fluorescence energy transfer biosensing of zinc," *Anal. Biochem.* **227**, 123–128 (1995).

[101] T. K. Hurst, D. Wang, R. B. Thompson, and C. A. Fierke, "Carbonic anhydrase II-based metal ion sensing: advances and new perspectives," *Biochim. Biophys. Acta (Proteins and Proteomics)* **1804**, 393–403 (2010).

[102] J. U. Sutter, D. J. S. Birch, and O. J. Rolinski, "CdSe/ZnS core/shell quantum dots as luminescence lifetime sensors for Cu^{2+}," *Meas. Sci. Technol.* **23**, 055103 (2012).

[103] M. Bruchez Jr, M. Moronne, P. Gin, S. Weiss, and A. P. Alivisatos, "Semiconductor nanocrystals as fluorescent biological labels," *Science* **281**, 2013–2015 (1998).

[104] A. R. Clapp, I. L. Medintz, J. M. Mauro, R. F. Brent, M. G. Bawendi, and H. Mattoussi, "Fluorescence resonance energy transfer between quantum dot donors and dye-labelled protein acceptors," *J. Am. Chem. Soc.* **126**, 301–310 (2004).

[105] R. Y. Tsien, "The green fluorescent protein," *Annu. Rev. Biochem.* **67**, 67509–67544 (1998).

[106] A. J. W. G Visser, S. P. Laptenok, N. V. Visser, A. van Hoek, D. J. S. Birch, J.-C. Brochon, and J. W. Borst, "Time-resolved FRET fluorescence spectroscopy of visible fluorescent protein pairs," *Eur. Biophys. J.* **39**, 241–253 (2010).

[107] R. F. Steiner, "Fluorescence anisotropy: theory and applications," in *Topics in Fluorescence Spectroscopy*, edited by J. R. Lakowicz (Plenum Press, New York, 1991), Vol. 2, pp. 1–52.

[108] A. Kawski, "Fluorescence anisotropy: theory and applications of rotational depolarization," *Crit. Rev. Anal. Chem.* **23**(6), 459–529 (1993).

[109] M. D. Barkley, A. A. Kowalczyk, and L. Brand, "Fluorescence decay studies of anisotropic rotations of small molecules," *J. Chem. Phys.* **75**(7), 3581–3593 (1981).

[110] D. J. S. Birch and C. D. Geddes, "Sol-gel particle growth studied using fluorescence anisotropy: an alternative to scattering techniques," *Phys. Rev. E* **62**, 2977–2980 (2000).

[111] M. P. Heyn, "Determination of lipid order parameters and rotational correlation times from fluorescence depolarization experiments," *FEBS Lett.* **108**(2), 359–364 (1979).

[112] G. Porter, P. J. Sadkowski, and C. J. Tredwell, "Picosecond rotational diffusion in kinetic and steady state fluorescence spectroscopy," *Chem. Phys. Lett.* **49**(3), 416–420 (1977).

[113] H. J. Eichler, U. Klein, and D. Langhans. Measurement of orientational relaxation times of rhodamine 6G with a streak camera," *Chem. Phys. Lett.* **67**(1), 21–23 (1979).

[114] R. Wijnaendts Van Resandt and L. De Maeyer, "Picosecond rotational diffusion by differential single-photon fluorescence spectroscopy," *Chem. Phys. Lett.* **78**(2), 219-223 (1981).

[115] U. Narang, R. Wang, P. N. Prasad, and F. V. Bright, "Effect of aging on the dynamics of rhodamine 6G in tetramethyl orthosilicate-derived sol-gels," *J. Phys. Chem.* **98**, 17–22 (1994).

[116] C. D. Geddes, J. Karolin, and D. J. S. Birch, "1 and 2-photon fluorescence anisotropy decay in silicon alkoxide sol-gels: interpretation in terms of self-assembled nanoparticles," *J. Phys. Chem.* **106**, 3835–3841 (2002).

[117] M. Ameloot, M. vandeVen, A. U. Acuña, and B. Valeur, "Fluorescence anisotropy measurements in solution: methods and reference materials," *Pure Appl. Chem.* **85**, 589–608 (2013).

[118] B. R. Lentz, "Membrane 'fluidity' as detected by diphenylhexatriene probes," *Chem. Phys. Lipids* **50**, 171–190 (1989).

[119] P. Yip, J. Karolin, and D. J. S. Birch, "Fluorescence anisotropy metrology of electrostatically and covalently labelled silica nanoparticles," *Meas. Sci. Technol.* **23**, 084003 (2012).

[120] K. Apperson, J. Karolin, R. W. Martin, and D. J. S. Birch, "Nanoparticle metrology standards based on the time resolved fluorescence anisotropy of silica colloids," *Meas. Sci. Technol.* **20** 025310 (2009).

[121] A. Bruno, C. de Lisio, P. Minutolo, and A. D'Alessio, "Characterization of ultrafast fluorescence from nanometric carbon particles," *J. Opt. A. Pure Appl. Opt.* **10**, S578–S584 (2008).

[122] L. Brand, J. R. Knutson, L. Davenport, J. M. Beecham, R. E. Dale, D. G. Walbridge, and A. A. Kowalczyk, "Time-resolved fluorescence spectroscopy: some applications of associative behavior to studies of proteins and membranes," in *Spectroscopy and the Dynamics of Biological Systems*, edited by P. Bayler and R. E. Dale (Academic Press, London, 1985), pp. 259–305.

[123] T. A. Smith, M. Irwanto, D. J. Haines, K. P. Ghiggino, and D. P. Millar, "Time-resolved fluorescence anisotropy measurements of the adsorption of rhodamine B and a labeled polyelectrolyte onto colloidal silica," *Colloid Polym. Sci.* **276**, 1032–1037 (1998).

[124] R. B. Thompson, B. P. Maliwal, and V. L. Feliccia, "Determination of picomolar concentrations of metal ions using fluorescence anisotropy: biosensing with a 'reagentless' enzyme transducer," *Anal. Chem.* **70**(22), 4717–4723 (1998).

[125] Z. Gryczynski, O. O. Abugo, and J. R. Lakowicz, "Polarization sensing of fluorophores in tissues for drug compliance monitoring," *Anal. Biochem.* **273**, 204–211 (1999).

[126] D. Allsop, L. Swanson, S. Moore, Y. Davies, A. York, O. M. A. El-Agnaf, and I. Soutar, "Fluorescence anisotropy: a method for early detection of Alzheimer beta-peptide (A beta) aggregation," *Biochem. Biophy. Res. Commun.* **285**, 58–62 (2001).

[127] D. Tleugabulova, A. M. Duft, M. A. Brook, and J. D. Brennan, "Monitoring solute interactions with poly(ethylene oxide)-modified colloidal silica nanoparticles via fluorescence anisotropy decay," *Langmuir* **20**, 101–108 (2004).

[128] A. Cleary, J. Karolin, and D. J. S. Birch, "pH tracking of silica hydrogel nanoparticle growth," *Appl. Phys. Lett.* **89**, 113125–113127 (2006).

[129] W. Denk, J. H. Strickler, and W. W. Webb, "Two-photon laser scanning fluorescence microscopy," *Science* **248**, 73–76 (1990).

[130] V. E. Centonze and J. G. White, "Multiphoton excitation provides optical sections from deeper within scattering specimens than confocal imaging," *Biophys. J.* **75**, 2015–2024 (1998).

[131] A. Diaspro, G. Chirico, and M. Collini, "Two-photon fluorescence excitation and related techniques in biological microscopy," *Quart. Rev. Biophys.* **38**, 97–166 (2005).

[132] D. J. S. Birch, "Multiphoton excited fluorescence spectroscopy of biomolecular systems," *Spectrochim. Acta.* **57**, 2313–2336 (2001).

[133] N. L. Thompson and J. K. Pero, "Total internal reflection microscopy: applications in biophysics," in *Fluorescence Spectroscopy in Biology*, edited by O.S. Wolfbeis, M. Hof, R. Hutterer and V. Fidler (Springer, Berlin, 2005), pp. 79–103.

[134] A. M. Macmillan, J. Karolin, D. Panek, C. D. McGuinness, J. C. Pickup, D. Graham, W. E. Smith, and D. J. S. Birch, "Improved biocompatibility of protein encapsulation in sol-gel materials," *J. Sol-Gel Sci. Technol.* **49**, 380–384 (2009).

[135] N. Thompson, "Fluorescence correlation spectroscopy," in *Topics in Fluorescence Spectroscopy*, edited by J. R. Lakowicz (Plenum Press, New York, 1991), Vol. 2, pp. 337–378.

[136] J. Mertz, C. Xu, and W. W. Webb, "Single-molecule detection by two-photon excited fluorescence," *Opt. Lett.* **20**(24), 2532–2534 (1995).

[137] J. K. Trautman, J. J. Macklin, L. E. Brus, and E. Betzig, "Near-field spectroscopy of single molecules at room temperature," *Nature* **369**, 40–42 (1994).

[138] X. Sunney Xie and R. C. Dunn, "Probing single molecule dynamics," *Science* **265**, 361–364 (1994).

[139] W. E. Moerner, and D. P. Fromm, "Methods of single-molecule fluorescence spectroscopy and microscopy," *Rev. Sci. Instrum.* **74**, 3597–3619 (2003).

[140] M. Kumbhhakar, S. Nath, T. Mukherjee, J. P. Mittal, and H. Pal, "Single-molecule detection in exploring nanoenvironments: an overview," *J. Photochem. Photobiol C. Photochem. Rev.* **5**, 113–137 (2004).

[141] J. Hohlbein, K. Gryte, M. Heilemann, and A. N. Kapanidis, "Surfing on a new wave of single molecule fluorescence methods," *Phys. Biol.* **7**, 031001-22 (2010).

[142] D. Pánek. "Developments for Single Molecule Studies," PhD thesis, University of Strathclyde, Glasgow, UK, 2011.

[143] T. Ha and P. Tinnefeld, "Photophysics of fluorescent probes for single-molecule biophysics and super-resolution imaging," *Annu. Rev. Phys. Chem.* **63**, 595–617 (2012).

[144] M. A. Thompson, M. D. Lew, and W. E. Moerner, "Extending microscopic resolution with single-molecule imaging and active control," *Annu. Rev. Biophys.* **41**, 321–342 (2012).

[145] S. W. Hell and J. Wichmann, "Breaking the diffraction resolution limit by stimulated emission: stimulated-emission-depletion fluorescence microscopy," *Opt. Lett.* **19**(11), 780–782 (1994).

[146] E. Betzig, G. H. Patterson, R. Sougrat, O. W. Lindwasser, S. Olenych, J. S. Bonifacino, M. W. Davidson, J. Lippincott-Schwartz, and H. F. Hess, "Imaging intracellular fluorescent proteins at nanometer resolution," *Science* **313**, 1642–1645 (2006).

[147] M. J. Rust, M. Bates, and X. Zhuang, "Stochastic optical reconstruction microscopy (STORM) provides sub-diffraction-limit image resolution," *Nat. Meth.* **3**, 793–795 (2006).

[148] S. T. Hess, T. P. K. Girirajan, and M. D. Mason, "Ultra-high resolution imaging by fluorescence photoactivation localization microscopy," *Biophys. J.* **91**, 4258–4272 (2006).

[149] D. Aquino, A. Schönle, C. Geisler. C. Middendorff, C. A. Wurm, Y. Okamura, T. Lang, S. W. Hell, and A. Egner, "Two-color nanoscopy of three-dimensional volumes by 4Pi detection of stochastically switched fluorophores," *Nat. Meth.* **8**(4), 353–359 (2011).

[150] M. G. Gustafsson, "Surpassing the lateral resolution limit by a factor of two using structured illumination microscopy," *J. Microsc.* **198**(Pt 2), 82–87 (2000).

[151] E. J. Rees, M. Erdelyi, D. Pinotsi, A. Knight, D. Metcalf, and C. F. Kaminski, "Blind assessment of localization microscope image resolution," *Opt. Nanosc.* **1**, 1–12 (2012).

[152] M. Heilemann, S. van de Linde, Schüttpelz, R. Kasper, B. Seefeldt, A. Mukherjee, P. Tinnefeld, and M. Sauer, "Subdiffraction-resolution fluorescence imaging with conventional fluorescent probes," *Angew Chem. Int. Ed.* **47**, 6172–6176 (2008).

[153] M. A. J. Rodgers, and P. A. Firey, "Instrumentation for fluorescence microscopy with picosecond time resolution," *Photochem. Photobiol.* **42**(5), 613–616 (1985).

[154] X. F. Wang, A. Periasamy, and B. Herman, "Fluorescence lifetime imaging microscopy (FLIM): instrumentation and applications," *Crit. Rev. Anal. Chem.* **23**(5), 369–395 (1992).

[155] T. French, P. T. C. So, C. Y. Dong, K. M. Berland, and E. Gratton, "Fluorescence lifetime imaging techniques for microscopy," *Meth. Cell. Biol.* **56**, 277–304 (1998).

[156] J. W. Borst, and A. J. W. G. Visser, "Fluorescence lifetime imaging microscopy in life sciences," *Meas. Sci. Technol.* **21**, 102002 (2010).

[157] G. S. Buller, and R. J. Collins, "Single-photon generation and detection," *Meas. Sci. Technol.* **21**, 012002 (2010).

[158] A. Periasamy, "Fluorescence energy transfer microscopy: a mini review," *J. Biomed. Opt.* **6**(3), 287–291 (2001).

[159] K. Suhling, P. M. W. French, and D. Phillips, "Time-resolved fluorescence microscopy," *Photochem. Photobiol.* **4**, 13–22 (2005).

[160] T. L. Doane, and C. Burda, "The unique role of nanoparticles in nanomedicine: imaging, drug delivery and therapy," *Chem. Soc. Rev.* **41**, 2885–2911 (2012).

[161] V. Biju, T. Itoh, A. Anas, A. Sujith, and M. Ishikawa, "Semiconductor quantum dots and metal nanoparticles: syntheses, optical properties, and biological applications," *Anal. Bioanal. Chem.* **391**, 2469–2495 (2008).

[162] J. R. Lakowicz, Y. B. Shen, S. D'Auria, J Malicka, J. Y. Fang, and Z. Gryczynski, "Effects of silver island films on fluorescence intensity, lifetimes, and resonance energy transfer," *Anal. Biochem.* **301**(2), 261–277 (2002).

[163] J. R. Lakowicz, "Radiative decay engineering: biophysical and biomedical applications," *Anal. Biochem.* **298**(1), 1–24 (2001).

[164] R. Tantra and A. Knight, "Cellular uptake and intracellular fate of engineered nanoparticles: a review on the application of imaging techniques," *Nanotoxicology* **5**(3), 381–392 (2011).

[165] J. P. Wilcoxon, J. E. Martin, F. Parsapour, B. Wiedenman, and D. F. Kelley, "Photoluminescence from nanosize gold clusters," *J. Chem. Phys.* **108**(21), 9137–9143 (1998).

[166] M. B. Mohamed, V. Volkov, S. Link, and M. A. El-Sayed. "The 'lightening' gold nanorods: fluorescence enhancement of over a million compared to gold metal," *Chem. Phys. Lett.* **317**, 517–523 (2000).

[167] R. A. Farrer, F. L. Butterfield, V. W. Chen, and J. T. Fourkas, "Highly efficient multiphoton-absorption-induced luminescence from gold nanoparticles," *Nano Lett.* **5**(6), 1139–1142 (2005).

[168] K. Imura, T. Nagahara, and H. Okamoto, "Near-field two-photon-induced photoluminescence from single gold nanorods and imaging of plasmon modes," *J. Phys. Chem. B* **109**(27), 13214–13220 (2005).

[169] D. M. Chevrier, A. Chatt, and P. Zhang, "Properties of protein-stabilized fluorescent gold nanoclusters: short review," *J. Nanophoton.* **6**, 064504-01–064504-16 (2012).

[170] J. Murphy, T. K. Sau, A. M. Gole, C. J. Orendorff, J. Gao, L. Gou, S. E. Hunyadi, and T. Li, "Anisotropic metal nanoparticles: synthesis, assembly, and optical applications," *J. Phys. Chem. B* **109**, 13857–13870 (2005).

[171] X. Huang, S. Neretina, and M. A. El-Sayed, "Gold nanorods: from synthesis and properties to biological and biomedical applications," *Adv. Mater.* **21**, 4880–4910 (2009).

[172] R. Sardar, A. M. Funston, P. Mulvaney, and R. W. Murray, "Gold nanoparticles: past, present, and future," *Langmuir* **25**(24), 13840–13851 (2009).

[173] Y. Zhang, J. Yu, D. J. S. Birch, and Y. Chen, "Gold nanorods for fluorescence lifetime imaging in biology," *J. Biomed. Opt.* **15**(2), 020504-3 (2010).

[174] O. P. Varnavski, M. B. Mohamed, M. A. El-Sayed, and T. Goodson III, "Relative enhancement of ultrafast emission in gold nanorods," *J. Phys. Chem. B.* **107**, 3101–3104 (2003).

[175] P. Biagioni, M. Celebrano, M. Savoini, G. Grancini, D. Brida, S. Mátéfi-Tempfli, M. Mátéfi-Tempfli, L. Duò, B. Hecht, G. Cerullo, et al., "Dependence of the two-photon photoluminescence yield of gold nanostructures on the laser pulse duration," *Phys. Rev. B* **80**, 045411-5 (2009).

[176] Y. Zhang, D. J. S. Birch, and Y. Chen, "Two-photon excited surface plasmon enhanced energy transfer between DAPI and gold nanoparticles: opportunities in intra-cellular imaging and sensing," *App. Phys. Lett.* **99**, 103701-3 (2011).

[177] C. V. Durgadas, C. P. Sharma, and K. Sreenivasan, "Fluorescent gold clusters as nanosensors for copper ions in live cells," *Analyst* **136**, 933–940 (2011).

[178] D. J. S. Birch, "Fluorescence detections and directions," *Meas. Sci. Technol.* **22**,052002 (2011).

[179] Y. Engelborough and A. J. W. G. Visser (eds.), *Fluorescence Spectroscopy and Microscopy Methods and Protocols* (Springer, New York, 2013).